Revision 2

Texture, geochemistry and geochronology of titanite and pyrite: Fingerprint of magmatic-hydrothermal fertile fluids in the Jiaodong Au province

Xing-Hui Li[1,2], Hong-Rui Fan[1,2,3,*], Ri-Xiang Zhu[2,3,4], Matthew Steele-MacInnis[5], Kui-Feng Yang[1,2,3], Cai-Jie Liu[6]

[1]*Key Laboratory of Mineral Resources, Institute of Geology and Geophysics, Chinese Academy of Sciences, Beijing 100029, China*

[2]*Innovation Academy for Earth Science, Chinese Academy of Sciences, Beijing 100029, China*

[3]*College of Earth and Planetary Science, University of Chinese Academy of Sciences, Beijing 100049, China*

[4]*State Key Laboratory of Lithospheric Evolution, Institute of Geology and Geophysics, Chinese Academy of Sciences, Beijing 100029, China*

[5]*Department of Earth and Atmospheric Sciences, University of Alberta, Edmonton, AB T6G 2E3, Canada*

[6]*No. 6 Institute of Geology and Mineral Resources Exploration of Shandong Province, Zhaoyuan 265400, China*

*Corresponding author. Tel.: +86 10 82998218; fax: +86 10 62010846. E-mail address: fanhr@mail.iggcas.ac.cn (H.-R., Fan).

ABSTRACT

The Au mineralization in the giant Jiaodong Au province is enigmatic and difficult to fit current classic mineralization models, primarily because of uncertainties as to the sources of ore-forming fluids and metals. The ca. 120 Ma Au mineralization has been previously proposed to have occurred during a magmatic lull, which would negate a magmatic-hydrothermal genetic model. However, recent drilling has revealed a buried mineralized monzonite equivalent in age to the Au mineralization, in the Linglong goldfield. Here, we present comprehensive textural, geochemical (LA-(MC)-ICPMS trace element, Nd and S isotopes) and geochronological (LA-ICPMS U-Pb dating) analyses of titanite and pyrite from this previously unrecognized monzonite. Three types of titanite were distinguished, including magmatic Ttn1 and hydrothermal Ttn2 and Ttn3, which show indistinguishable U-Pb ages (120.7 ± 3.1 Ma and 120.9 ± 2.6 Ma), REE patterns and Nd isotopes ($\varepsilon_{Nd}(t)$ = -14.7 to -12.9), implying that hydrothermal fluids were directly exsolved from the monzonitic magma, contemporaneous with the large-scale Au mineralization at ca. 120 Ma. The Nd isotopes of titanite potentially indicate a lower crustal source mixed with mantle materials for the monzonite. Four types of pyrite were analyzed, including magmatic Py1 from the fresh biotite monzonite, hydrothermal Py2 from the altered biotite monzonite, hydrothermal Py3 from quartz-pyrite veins with a monazite U-Pb age of 118.2 ± 4.6 Ma, and magmatic Py4 from mafic enclaves of the Gushan granite at ca.120 Ma. The $\delta^{34}S$ values of magmatic Py1 and Py4

(+1.9 to +6.3 ‰, and +5.0 to +6.4 ‰, respectively) and hydrothermal Py2 and Py3 (+6.4 to +9.5 ‰, and +6.5 to +7.6 ‰, respectively) are consistent with sulfur isotopic fractionation between melt and fluid. Hydrothermal Py2 and Py3 also have higher Co, As, Ag, Sb and Bi contents and submicron gold inclusions, implying that the magmatic-hydrothermal fluids were fertile for mineralization. This study highlights the importance of monzonite magmatism and exsolved fertile fluids in regional Au mineralization. Hydrous magmas at ca.120 Ma probably extracted Au efficiently from the lower crustal-mantle sources and released auriferous fluids at the late magmatic stage, leading to the formation of Au deposits in the Jiaodong province.

Keywords: Titanite, pyrite, monazite, biotite monzonite, U-Pb geochronology, magmatic-hydrothermal fluid

INTRODUCTION

The Early Cretaceous Au deposits in the Jiaodong Peninsula constitute the largest Au province of China, containing more than 5000 tons of proven Au resources. Mineralization in the Jiaodong Peninsula is considered unique relative to the accepted model for orogenic Au deposits (e.g., Groves et al., 1998), in that Au mineralization postdates the Precambrian metamorphic wallrocks by about 2 billion years (Goldfarb and Santosh 2014). Numerous studies have defined the ore-controlling structures, hydrothermal alterations, ore-fluid chemistry, hydrothermal processes and fluid evolution of both disseminated- to stockwork-style and auriferous quartz-pyrite vein-type Au deposits across the Jiaodong Peninsula (Fan et al. 2003, 2007; Li et al. 2012a; Goldfarb and Santosh 2014; Mills et al. 2015; Deng et al. 2015, 2020b; Feng et al. 2018, 2020; Li et al. 2018). The timing of Au mineralization has also been well constrained to 120 ± 5 Ma by Rb-Sr dating of pyrite, $^{40}Ar/^{39}Ar$ dating of hydrothermal muscovite and U-Pb dating of hydrothermal monazite (Yang and Zhou 2001; Ma et al. 2017; Li et al. 2018; Zhang et al. 2020; Deng et al. 2020a). Nevertheless, the genesis of the Jiaodong Au province is contentious, given the failure of current models of mineralization to account for its features. This debate is primarily rooted in uncertainties as to the sources of ore-forming fluids and metals, and particularly their genetic relationship(s) to Mesozoic magmatism, Precambrian metamorphic host rocks, subducted slab and sediment, and/or metasomatized lithosphere (Zhai et al. 2004; Chen et al. 2005;

Goldfarb and Santosh 2014; Zhu et al. 2015; Deng et al. 2015, 2020b; Wang et al. 2020).

Two main problems obstruct linking Au mineralization to the widespread granitic magmatism in the Jiaodong Au province. Firstly, a time gap of at least ~8 million years separates the ages of mineralization and of known magmatism (Li et al. 2019a; Deng et al. 2020a). Secondly, direct evidence for a genetic affinity between magmatism and hydrothermal mineralization has been hitherto lacking. However, recent deep drilling projects in the Linglong goldfield, one of the largest Au-producing districts in the Jiaodong Au province, discovered a buried mineralized biotite monzonite that shows petrographic features distinct from those of the exposed Mesozoic granitoids (Linglong, Luanjiahe, Guojialing and Aishan granites). Shen et al. (2016) constrained the emplacement age of the monzonite to ca. 124 Ma by $^{40}Ar/^{36}Ar$ dating of biotite, and suggested a temporal relationship between the monzonite and Au mineralization. The monzonite is nearly contemporaneous with the regional Gushan granite, which has a zircon U-Pb age of 120-119 Ma (Li et al. 2012b). Thus, this newly discovered monzonite suggests a potentially extensive episode of magmatism during this period. Moreover, the mineralized monzonite shows distinctive hydrothermal features, suggesting a relationship between magmatic-hydrothermal fluids and mineralization. As such, the mineralized monzonite provides a good opportunity to evaluate the role of magmatism and magmatic-hydrothermal fluid release in the ore-forming process, and to explore the

sources of ore-forming fluids and metals, in the Jiaodong Au province.

Several magmatic-hydrothermal minerals are present in the monzonite, including titanite, monazite, pyrite, pyrrhotite and magnetite. Titanite commonly contains sufficient uranium contents for precise U-Pb dating and has been widely used to date magmatic and hydrothermal events (Frost et al. 2001; Li et al. 2010; Xiao et al. 2021). Incorporation of minor and trace elements, such as V, Mn, Cu, Zr, REE, Hf, Pb, Th and U, in titanite is sensitive to temperature, pressure, oxygen fugacity, and melt and fluid compositions. As such, titanite can be a valuable indicator of magmatic and hydrothermal conditions (Hayden et al. 2008; Xie et al. 2010; Cao et al. 2015; Xiao et al. 2021). The trace elements and sulfur isotopes of pyrite and pyrrhotite can be used to discriminate different sulfur sources and genetic environments, and to understand the physicochemical conditions of sulfide deposition (Deditius et al. 2014; Peterson and Mavrogenes 2014; Tanner et al. 2016; Li et al. 2018). Similarly, magnetite is stable over a wide range of magmatic-hydrothermal conditions and has been used to derive insights on petrogenetic discrimination, physicochemical conditions, and the magma fertility (Dare et al. 2014; Zhi et al. 2019; Dora et al. 2020). The geochemistry of these magmatic-hydrothermal minerals, when integrated with detailed microtextural studies, is useful in fingerprinting magmatic and hydrothermal processes.

Here, we document results of detailed textural studies, *in situ* U-Pb geochronology and trace-element and isotope geochemistry of magmatic-

hydrothermal titanite, monazite, pyrite, pyrrhotite and magnetite from the mineralized biotite monzonite, as well as pyrite in mafic enclaves from the Gushan pluton. Our results provide insight into: (1) the temporal relationship between the monzonite and Au mineralization; (2) the link between magmatic and hydrothermal events; (3) the mineralization potential of the monzonite; and (4) the sources of the ore-forming fluids and metals in the Jiaodong Au province.

GEOLOGIC BACKGROUND

Regional geology

The Jiaodong Peninsula is located at the southeastern margin of the North China Craton (NCC), bounded by the crustal-scale Tancheng-Lujiang (Tan-Lu) fault to the west. The peninsula comprises the Jiaobei Terrane in the northwest and the Sulu ultrahigh-pressure metamorphic (UHP) belt in the southeast, which are separated by the Wulian−Yantai Fault (Zhou et al. 2008; Fig. 1). The northern Jiaobei Uplift on the Jiaobei Terrane is dominated by Precambrian metamorphic basement, including the Neoarchean Jiaodong Group, the Paleoproterozoic Jingshan and Fenzishan Groups, and the Neoproterozoic Penglai Group. These rocks were intruded by widespread middle-late Mesozoic granitoids (the Jurassic Linglong and Luanjiahe granite at 160-159 Ma, the Cretaceous Guojialing granodiorite at 130-126 Ma, Gushan granite at 120-119 Ma and Aishan-Sanfoshan granite at 118-115 Ma; Miao et al. 1997; Goss et al. 2010; Li et al. 2012b; Yang et al. 2012; Li et al. 2019a; Fig. 1), whereas the

148 southern Jiaolai Basin is filled with Cretaceous sedimentary and volcanic rocks
149 (Liu et al. 2009; Xie et al. 2012). The Sulu UHP belt mainly consists of
150 Neoproterozoic granitic gneisses, Triassic UHP metamorphic rocks and
151 Jurassic-Cretaceous granitoids (Zheng 2008; Xu et al. 2016). Structurally, the
152 Jiaodong Peninsula is dominated by NE- to NNE-trending brittle-ductile shear
153 zones with sinistral-oblique-reverse movements in the Late Jurassic, followed
154 by late reactivation and development of brittle normal faults in the Early
155 Cretaceous (Sun et al. 2007; Deng et al. 2015).

156 Deposits in the Jiaodong Au province are divided into three belts from west
157 to east: the Zhaoyuan−Laizhou, Penglai−Qixia and Muping−Rushan belts. The
158 deposits are distributed along regional second- or third- order NE- to NNE-
159 trending faults of the Tan−Lu fault system, particularly the Sanshandao-
160 Cangshang, Jiaojia-Xincheng, Zhaoyuan-Pingdu, Qixia and Muping-Rushan
161 faults (Fig. 1; Fan et al. 2007). The majority of Au deposits, dated at 120 ± 5
162 Ma, are hosted within the widespread Jurassic Linglong, Luanjiahe and
163 Kunyushan granites, Cretaceous Guojialing granodiorite and Precambrian
164 metamorphic rocks (e.g., Yang and Zhou 2001; Fan et al. 2003; Li et al. 2012a,
165 2018; Zhang et al. 2020; Deng et al. 2020a). Quartz-sulfide vein-type and
166 disseminated/stockwork-type Au mineralization account for most of the Au
167 resources in the Jiaodong Au province. These deposits are thought to have
168 formed within the same tectonic setting, but under different local stress fields
169 (Qiu et al. 2002; Yang et al. 2018). Of the three belts, the Zhaoyuan-Laizhou

belt is the most significant in terms of endowment, hosting over 85% of Au resources in the district.

Ore geology and petrography

The Linglong goldfield, which contains several large Au deposits such as Linglong, Jiuqu and Dongfeng, is located to the east of the Zhaoyuan-Laizhou Au belt and at the northern tip of the Zhaoyuan-Pingdu fault (Fig. 1). This goldfield is typified by the quartz-sulfide vein-type mineralization, with minor disseminated sulfide replacements and stockworks. Hundreds of auriferous quartz veins are present in this goldfield, occurring in steeply dipping, NE- to NNE-trending fractures in the hanging wall of the Zhaoyuan-Pingdu fault. The mineralized veins are mainly hosted in the Jurassic Linglong and Luanjiahe granites, with fewer in the Cretaceous Guojialing granodiorite (Wen et al. 2015). The Zhaoyuan-Pingdu fault is intersected by the NEE-trending Potouqing fault and crosscut by the NNE-trending Linglong fault, both of which control the occurrence of ore bodies and the widespread emplacement of intermediate to mafic dykes.

The mineralized biotite monzonite was found in drill cores 72ZK1 and 72ZK2, at depths of 2070 m and 2374 m separately in the Linglong goldfield, and was suggested as a buried intrusion into the Jurassic Linglong and Luanjiahe granite (Fig. 2; Shen et al. 2016). The biotite monzonite is dark gray to light grayish green, massive, and medium-to-fine grained. Pyrite, pyrrhotite and magnetite are evenly distributed in the monzonite, with some grains

occurring as clusters (Fig. 3a-d, g). The mineral assemblage of the monzonite mainly comprises K-feldspar (35-40%), plagioclase (20-25%) and biotite (15-20%) (Fig. 3g, h). Other minerals include quartz (5-10%), amphibole (<5%), titanite, and minor zircon, allanite, apatite. Some coarse grains of K-feldspar and plagioclase have been altered to clay minerals, sericite and chlorite (Fig. 3h).

Silicification, sericitization and carbonation occurred in the biotite monzonite near the intrusive contact with the overlying Jurassic Luanjiahe granite, whereas unaltered rocks were present at greater depth. The alteration is characterized mostly by addition of quartz, sericite, chlorite and calcite. Several quartz-pyrite veinlets are observed in the overlying Luanjiahe granite (Fig. 3e), suggesting a hydrothermal event probably related to the emplacement and degassing of the monzonitic magma.

The Gushan granite, located in the southwest of the Linglong goldfield, approximately 35 km away from the drill core 72ZK1 (Fig. 1), intrudes the Jurassic Luanjiahe granite and carries mafic microgranular enclaves (MMEs, Fig. 3f). The MMEs are generally fine grained and contain dominantly hornblende, plagioclase, biotite, K-feldspar and quartz, with minor apatite and titanite. Some pyrite crystals, coexisting with magnetite and chalcopyrite, are found in the MMEs.

SAMPLES AND ANALYTICAL METHODS

Representative samples were collected from the drill core 72ZK1 in the

Linglong goldfield, including quartz-pyrite veinlets (19ZY09), silicified-sericitized-carbonated monzonite (19ZY01, 19ZY07, 19ZY13, 19ZY15) and fresh to weakly-altered biotite monzonite (19ZY03, 19ZY14) at depths 2056-2153 m. Samples of MMEs from the Gushan pluton were also analyzed. Petrographic studies were carried out on thin sections using field emission scanning electron microscope (FESEM). Titanite and hydrothermal monazite were analyzed for geochronology, major and trace element contents, and Nd isotopes using EPMA, LA-ICPMS and LA-MC-ICPMS. Pyrite, pyrrhotite and magnetite were selected for *in situ* trace elemental and/or sulfur isotopic analyses using LA-ICPMS and LA-MC-ICPMS. Except for FESEM and EPMA analyses, which were done at the Institute of Geology and Geophysics, Chinese Academy of Sciences (IGGCAS), other measurements were all conducted at the Wuhan Sample Solution Analytical Technology Co., Ltd., China.

In situ titanite U-Pb dating and geochemical analyses

The major element compositions of titanite were determined using a JEOL-JXA8100 electron microprobe. The operating conditions were 15 kV accelerating voltage, 10 nA beam current and 5 μm probe beam. Calibration standards used were diopside for Ca and Si, jadeite for Al and Na, garnet for Fe, bustamite for Mn, K-feldspar for K, tugtupite for Cl, and fluorite for F. The data were corrected using the atomic number-absorption-fluorescence (ZAF) method.

Prior to analytical works, titanite grains were carefully examined using

transmitted and reflected light microscopy and backscatter electron (BSE) images so as to avoid fractures, inclusions and U-rich domains. In addition, magmatic and hydrothermal titanites were distinguished preliminarily based on their occurrence, texture (oscillatory versus core-rim and irregular zoning) and mineral association. *In situ* U-Pb isotopes and trace elements of titanite were analyzed simultaneously by LA-ICPMS employing an Agilent 7900 ICP-MS with a Geolas HD laser ablation system. A spot size of 44 μm was used with pulse rate of 3 Hz and laser energy of 80 mJ. The Pb/U ratios were calibrated against the zircon standard 91500 (Wiedenbeck et al. 1995) and monitored according to the titanite standard MKED1 (Spandler et al. 2016). NIST 610 was used as an external standard, and average CaO concentrations of titanite determined by EPMA were used as the internal standard. Each analysis incorporated a background acquisition of approximately 20 s followed by 50 s of data acquisition. Details of the operating conditions, analytical method and data reduction process can be found in Liu et al. (2008). A Microsoft Excel-based spreadsheet ICPMSDataCal was used to perform off-line selection and integration of background and analyzed signal, time-drift correction and quantitative calibration for U-Pb dating and trace element analysis (Liu et al. 2008). Tera-Wasserburg Concordia diagrams and weighted mean calculations were made using Isoplot/Ex_ver3 (Ludwig 2003).

In situ Nd isotopes of titanite were measured on spots previously analyzed for U-Pb dating using a Neptune Plus multi-collector ICPMS, coupled with a

Geolas HD exciter ArF laser ablation system. A laser pulse energy of ~ 90 mJ, repetition rate of 8 Hz and spot size of 32 μm were used. The mass discrimination factor for $^{143}Nd/^{144}Nd$ was determined using $^{146}Nd/^{144}Nd$ (0.7219) with an exponential fractionation law. The ^{149}Sm signal was used to correct the remaining ^{144}Sm interference on ^{144}Nd, using the $^{144}Sm/^{149}Sm$ ratio of 0.2301. The mass fractionation of $^{144}Sm/^{149}Sm$ was corrected by the $^{147}Sm/^{149}Sm$ normalization, using the interference-free $^{147}Sm/^{149}Sm$ = 1.08680 and exponential law (Xu et al. 2015). The $\varepsilon_{Nd}(t)$ values were calculated relative to the chondritic uniform reservoir (CHUR) parameters of Jacobsen and Wasserburg (1980) (present-day $^{143}Nd/^{144}Nd$ = 0.512638 and $^{147}Sm/^{144}Nd$ = 0.1967) with $^{143}Nd/^{144}Nd$ renormalized to $^{146}Nd/^{144}Nd$ = 0.7219 (Hamilton et al. 1983; Bouvier et al. 2008).

In situ monazite U-Pb dating

In situ U-Pb dating of monazite was conducted using the same instruments and analytical methods described above for the titanite analyses. The spot size and frequency of the laser for U-Pb dating were set to 16 μm and 2 Hz. Monazite standard 44069 (Aleinikoff et al. 2006) and glass NIST610 were used as external standards for U-Pb dating and trace element calibration, respectively.

In situ trace element analyses of pyrite and magnetite

Trace element concentrations of pyrite and magnetite were analyzed by LA-ICPMS. Detailed operating conditions and data reduction are similar to description by Liu et al. (2008). An Agilent 7900 ICP-MS instrument equipped

with a Geolas HD laser ablation system was used to acquire ion signal intensities. A "wire" signal smoothing device is included in the laser ablation system (Hu et al. 2015). For trace element analyses of pyrite, the spot size and frequency of the laser were set to 32 μm and 5 Hz, respectively. The sulfide reference material of MASS-1 (USGS) was used as an external bracketing standard. The data quality was monitored by analyzing the NIST 610 reference glass and the MASS-1 as unknowns interspersed with the measurements of the samples. For magnetite, the spot size and frequency of the laser were set to 44 μm and 5 Hz, respectively. Trace element compositions were calibrated against various reference materials (BHVO-2G, BCR-2G and BIR-1G) without using an internal standard (Liu et al. 2008). Each analysis incorporated a background acquisition of approximately 20-30 s followed by 50 s of data acquisition. An Microsoft Excel-based spreadsheet ICPMSDataCal was used in the identical fashion as indicated for trace element measurements above (Liu et al. 2008).

In situ S isotope analyses of pyrite and pyrrhotite

In situ sulfur isotope analyses of pyrite and pyrrhotite were performed on a Neptune Plus MC-ICPMS equipped with a Geolas HD excimer ArF laser ablation system. Pyrite and pyrrhotite were both ablated using a large spot size (44 μm) and slow pulse frequency (2 Hz) to avoid the down-hole fractionation effect (Fu et al., 2016). 100 laser pulses were completed in one analysis. The laser fluence was kept constant at ~5 J/cm^2. The Neptune Plus was equipped with nine Faraday cups fitted with 10^{11} Ω resistors. Isotopes ^{32}S, ^{33}S and ^{34}S

were collected in Faraday cups using static mode. A standard-sample bracketing method was employed to correct for instrumental mass fractionation. To avoid matrix effects, a pyrite standard PPP-1 (Gilbert et al. 2014) was chosen as a reference material for correcting the natural pyrite and pyrrhotite (Fu et al. 2016). In addition, the in-house reference pyrite SP-Py-01 ($\delta^{34}S_{VCDT}$ = 2.0 ‰ ± 0.5 ‰) and pyrrhotite SP-Po-01 ($\delta^{34}S_{VCDT}$ = 1.4 ‰ ± 0.4 ‰) were analyzed repeatedly as unknown samples to verify the accuracy of the calibration method. Standard errors for PPP-1, SP-Py-01 and SP-Po-01 are ± 0.2 ‰ (2σ; N = 54), ± 0.2 ‰ (2σ; N = 20) and ± 0.2 ‰ (2σ; N = 4), respectively.

RESULTS

Textures and chemical compositions of titanite

Titanite crystals are ubiquitous in the biotite monzonite, showing a wide range of textures. These crystals are about 100-400 μm in length, euhedral to anhedral in shape. Three types of titanite were identified based on their occurrence, petrographic features and chemical compositions (Figs. 4, 5, and Supplementary Fig. A1). The titanite compositional data obtained during this study are provided in Supplementary Table 1.

Type 1 titanite (Ttn1) typically displays discrete, euhedral-subhedral and rhombus-shaped grains, and occurs as intergrowths with plagioclase, K-feldspar and biotite in the matrix. Oscillatory zoning is the most common and characteristic internal texture of Ttn1, consisting of alternating light and dark bands observed in BSE images (Fig. 4a, b). In some cases, Ttn1 also shows

sector zoning consisting of patchy dark, light and/or oscillatory zones (Fig. 4a). These features suggest that Ttn1 is of magmatic origin. Ttn1 shows limited ranges of CaO (27.7-29.1 wt.%), TiO_2 (34.6-37.9 wt.%) and SiO_2 (30.2-31.8 wt.%), and low contents of Al_2O_3 (0.94-2.23 wt.%), FeO (0.59-1.57 wt.%) and MnO (0.03-0.24 wt.%) (Fig. 5). Trace element data show that Ttn1 has low concentrations of total REE (ΣREE = 862-9228 ppm, average 4431 ppm) and HFSE (Nb + Ta + Zr + Hf = 227-4964 ppm, average 1733 ppm), together with slight enrichment of Light REE over Heavy REE (LREE/HREE = 2.8-17.8, average 8.5), low Lu/Hf ratios (0.1-0.6, average 0.3), and weakly negative Eu anomalies (Eu_N/Eu_N^* = 0.5-0.9, average 0.8) (Fig. 5, Supplementary Fig. A1). Ttn1 shows large variations in the contents of Pb (0.4-12.7 ppm, average 2.2 ppm), Th (1.8-398.8 ppm, average 94.0 ppm), U (0.3-518.2 ppm, average 57.6 ppm) and Y (60-2420 ppm).

Type 2 titanite (Ttn2) occurs as subhedral to anhedral crystals characterized by simple zoning comprising irregular bright cores and light-gray contrasting rims under BSE (Fig. 4c-e). This type of titanite commonly shares planar contacts with pyrite. Ttn2 tends to have lower CaO (24.6-28.6 wt.%), TiO_2 (31.1-37.1 wt.%) and SiO_2 (28.4-30.8 wt.%), but higher FeO (0.83-2.41 wt.%) and MnO (0.13-0.33 wt.%) relative to Ttn1 (Fig. 5). Ttn2 also shows significantly higher concentrations of REE (3221-37648 ppm, average 20766 ppm), HFSE (531-5040 ppm, average 2529 ppm), Y (633-4960 ppm, average 2643 ppm), Pb (0.7-12.9 ppm, average 5.6 ppm), Th (39.1-738.6 ppm, average

376.7 ppm), and U (4.8-291.5 ppm, average 86.0 ppm), but broadly similar enrichment of LREE over HREE with slightly higher ratios of LREE/HREE (11.7-30.3, average 21.4) and Lu/Hf (0.1-2.9, average 0.9) (Fig. 5, Supplementary Fig. A1). In addition, Ttn2 displays more prominent negative Eu anomalies (Eu_N/Eu_N^* = 0.3-0.7, average 0.50) than Ttn1.

Type 3 titanite (Ttn3) occurs as fine, irregular veins penetrating and overgrowing Ttn2 (Fig. 4f-h). Ttn3 commonly occurs together with calcite and displays dark gray color under BSE. Ttn3 has similar ranges of CaO (27.3-28.9 wt.%), TiO_2 (34.7-37.8 wt.%), SiO_2 (30.3-31.3 wt.%) and Al_2O_3 (0.98-2.05 wt.%) to Ttn1, but slightly higher contents of FeO (0.67-2.23 wt.%) and MnO (0.05-0.23 wt.%) (Fig. 5). The contents of trace elements of Ttn3 lie mostly between those of Ttn1 and Ttn2， with REE (ΣREE = 1173-28457 ppm, average 10144 ppm), HFSE (123-8136 ppm, average 2344 ppm), Pb (0.5-6.8 ppm, average 2.8 ppm), Th (14.8-511.2 ppm, average 157.4 ppm), U (1.7-197.0 ppm, average 36.3 ppm) and Y (197-5389 ppm, average 2049 ppm). Ttn3 also displays moderate Lu/Hf ratios (0.2-1.5, average 0.5), and a slight enrichment of LREE relative to HREE (LREE/HREE = 6.2-18.6, average 13.0), showing flat chondrite-normalized REE patterns with negative Eu anomalies (Eu_N/Eu_N^* = 0.2-1.1, average 0.6), similar to that of Ttn1 and Ttn2 (Supplementary Fig. A1).

Geochronology of the biotite monzonite and hydrothermal event

Titanite U-Pb ages

In situ titanite U-Pb isotopic data are provided in Table 1. Locations of representative points for U-Pb dating are shown in Fig. 4. The uncorrected data were plotted on Tera-Wasserburg Concordia diagrams (Fig. 6a, b), and a regression through these data yielded a lower-intercept age. The y-intercept represents the initial $^{207}Pb/^{206}Pb$ ratio which can be used to conduct ^{207}Pb-correction to calculate the corrected $^{206}Pb/^{238}U$ age (Aleinikoff et al. 2002). The magmatic titanites (Ttn1) define a lower-intercept age of 120.7 ± 3.1 Ma (2σ, n = 18, MSWD = 1.8) with initial $^{207}Pb/^{206}Pb$ = 0.8516. With this common Pb composition, a ^{207}Pb-correction was conducted. Ten points yield a weighted average $^{206}Pb/^{238}U$ age of 118.8 ± 2.2 Ma (MSWD = 1.3) (Fig. 6a), consistent within error with the lower-intercept age. However, eight points exhibit lower U and Pb with higher percentage of common Pb, plotting away from the lower intercept and resulting in greater experimental errors. They cannot yield convincing $^{206}Pb/^{238}U$ ages based on ^{207}Pb-correction, thus the lower-intercept age (120.7 ± 3.1 Ma) is used as the magmatic titanite age. The hydrothermal titanites (Ttn2 and Ttn3) give a lower-intercept age of 120.9 ± 2.6 Ma (2σ, n = 19, MSWD = 1.4) with initial $^{207}Pb/^{206}Pb$ = 0.8530. Fifteen points define a ^{207}Pb-corrected weighted average $^{206}Pb/^{238}U$ age of 117.9 ± 2.2 Ma (MSWD = 1.1) which is consistent with the lower-intercept age (Fig. 6b). The other four points, plotting away from the lower intercept, were failed to produce convincing $^{206}Pb/^{238}U$ ages, thus the lower-intercept age (120.9 ± 2.6 Ma) is used as the hydrothermal titanite age. It is noteworthy that the $^{206}Pb/^{238}U$ ages for Ttn2 and

Ttn3, as well as cores and rims in Ttn2, are indistinguishable, thus they were regarded as a whole during age analysis.

Monazite U-Pb ages

The *in situ* U-Pb data of 19 spots on monazite grains are presented in Table 1. All the analyzed monazite grains are associated or intergrown with pyrite in the quartz-pyrite veinlets (Fig. 4i), thus their crystallization ages represent the timing of the hydrothermal (vein-forming) event. The U-Pb data give a lower-intercept age of 119.0 ± 5.8 Ma (2σ, n = 19, MSWD = 1.1) on the Tera-Wasserburg Concordia diagram. The initial $^{207}Pb/^{206}Pb$ value is 0.7373. The ^{207}Pb-corrected weighted average $^{206}Pb/^{238}U$ age is 118.2 ± 4.6 Ma (MSWD = 0.2) which is consistent with the lower intercept age (Fig. 6c).

Nd isotopic composition of titanite

In situ Nd isotopic compositions of titanite are shown in Supplementary Table 1. The analyzed Ttn1, Ttn2 and Ttn3 show restricted and indistinguishable $\varepsilon_{Nd}(t = 121\ Ma)$ values of -14.7 to -13.0, -14.7 to -13.5, and -14.3 to -12.9 (Fig. 7).

Classification, trace-element and sulfur isotopic compositions of pyrite, magnetite and pyrrhotite

Based on occurrence, optical characteristics and mineral assemblages, four types of pyrite were recognized. The complete dataset of trace element concentrations and sulfur isotopes is given in Supplementary Table 2.

Type 1 pyrite (Py1) occurs in the fresh biotite monzonite. It is characterized

by isolated euhedral-anhedral crystals coexisting with magnetite, and contains inclusions of plagioclase, quartz and titanite (Fig. 8a, e). The Py1 contains uniformly low concentrations of Co (3-374 ppm), Ni (3-41 ppm), Cu (0-7.9 ppm), Zn (0-4.1 ppm), As (0.2-0.9 ppm), Ag (0-0.05 ppm), Sb (0-0.09 ppm), Au (0-0.03 ppm, with two outliers at 0.1 ppm and 0.14 ppm), Pb (0-8.5 ppm) and Bi (0-6.1 ppm) (Fig. 9). It commonly displays homogeneous textures on BSE images (Fig. 8e), contrasting with heterogeneous compositional textures of Py2 and Py3 (Fig. 8f, g). The $\delta^{34}S$ values of Py1 are relatively low with a large variation from +1.9 to +6.3 ‰ (average +4.7 ‰) (Fig. 10). The coexisting magnetite grains mostly plot within the magmatic magnetite region on the Ti vs. Ni/Cr diagram (Dare et al., 2014) with low Ni/Cr ratios (0.02-0.93) (Supplementary Fig. A2).

Type 2 pyrite (Py2) mostly occurs as anhedral clusters in the altered monzonite which shows significant sericitization and carbonation. The Py2 is commonly enclosed within and crosscut by pyrrhotite (Fig. 8b, f), suggesting that Py2 formed earlier than pyrrhotite. It is likely partly replaced by pyrrhotite, resulting in corroded grain boundaries and metasomatic-relict texture (Fig. 8b). Trace element data show that the contents of Co (0.1-4837 ppm), Ni (0-87.6 ppm), As (0.3-86.4 ppm), Ag (0-0.4 ppm), Sb (0-4.5 ppm), Au (0-0.09 ppm, with one outlier of 18.7 ppm), Pb (0-218 ppm) and Bi (0-9.9 ppm, with an outlier of 16.8 ppm) in Py2 have large variations and are higher than Py1 (Fig. 9). The $\delta^{34}S$ values of Py2 are +6.4 to +9.5 ‰ (average +8.4 ‰) (Fig. 10), which

434 are higher than Py1 but similar to the $\delta^{34}S$ values of pyrite from other deposits
435 in the Jiaodong Au province (+6 to +10 ‰; Mao et al. 2008; Feng et al. 2018;
436 Li et al. 2018; Deng et al. 2020b). The pyrrhotite has a $\delta^{34}S$ range of +6.9 to
437 +8.8 ‰ (average +7.9 ‰) that overlaps with range of Py2.

438 Type 3 pyrite (Py3) occurs as subhedral, rounded crystals in the quartz-
439 pyrite veins (Fig. 8c, g). The Py3 contains low concentrations of Co (0-98.6
440 ppm), Ni (0-116 ppm), Cu (0-0.5 ppm), Zn (0.4-0.9 ppm), Ag (0-0.3 ppm), Sb
441 (0-0.1 ppm), Au (0-0.01 ppm, with an outlier of 0.1 ppm), Pb (0-2.2 ppm) and
442 Bi (0-1.0 ppm, with an outlier of 19.9 ppm), but markedly high contents of As
443 (325-852 ppm) (Fig. 9). The $\delta^{34}S$ values of Py3 are +6.5 to +7.6 ‰ (average
444 +7.2 ‰), which is entirely with the range of Py2 (Fig. 10).

445 Another type of pyrite (Py4) was sampled from the mafic enclaves of the
446 Gushan granite. It occurs as euhedral to anhedral crystals in the matrix and
447 commonly coexists with magnetite and minor chalcopyrite (Fig. 8d, h). Most of
448 the trace elements, including Co, Cu, Zn, As, Sb, Au, Pb and Bi, show low
449 concentrations (mostly below detection limits), but the contents Ag (0-2.85 ppm)
450 and Ni (227-3407 ppm) are relatively high and vary widely. The Py4 displays a
451 low and narrow range of $\delta^{34}S$ values from +5.0 to +6.4 ‰ (average +5.9 ‰)
452 (Fig. 10).

453 # DISCUSSION

454 ## Origins of the different generations of titanite

455 Distinct origins of titanite can be discriminated by their textures,

paragenetic mineral assemblages and chemical compositions (Cao et al. 2015; Fu et al. 2016). The Ttn1 grains are mostly euhedral and rhombus-shaped, show oscillatory and sector zoning under BSE, and occur as intergrowths with igneous plagioclase, K-feldspar and biotite in the matrix of the biotite monzonite, implying a magmatic origin. In contrast, the Ttn2 and Ttn3 grains are mostly subhedral to anhedral, show core-rim texture and penetrating relationship under BSE, and commonly show planar contacts with hydrothermal pyrite, sericite and calcite, suggesting a hydrothermal origin. This conclusion is further supported by the chemical compositions of the titanite grains. As demonstrated in Fig. 5, Ttn1 shows low Fe, Mn, REE and high Ti, Ca. The Ttn1 data fall in relatively restricted portions of these four diagrams, resembling typical magmatic titanite. In contrast, Ttn2 and Ttn3 are much more compositionally diverse, with relatively higher Fe, Mn, REE and lower Ti, Ca contents: all characteristics of hydrothermal titanite (Morad et al. 2009; Fu et al. 2016). The high Fe and Mn contents of Ttn2 and Ttn3 are consistent with Fe-rich hydrothermal fluids from which pyrite and pyrrhotite formed. Overall, Fig. 5a and 5c show negative correlations between TiO_2 and FeO, CaO and REE, respectively, indicating that appreciable amounts of Fe and REE substitute for Ti and Ca in the titanite structure, which is common in hydrothermal titanite (Cao et al. 2015; Li et al. 2020). The dominant substitution mechanisms are likely to be: $(Al, Fe)^{3+} + (F, OH)^{-} = Ti^{4+} + O^{2-}$, in which the substitution of Fe for Ti predominates, and $REE^{3+} + (Al, Fe)^{3+} = Ca^{2+} + Ti^{4+}$ (Olin and Wolff 2012;

Xie et al. 2010).

Our results indicate that the concentrations of trace elements, including REE, HFSE, Th, U and Pb, are quite distinct between magmatic (Ttn1) and hydrothermal (Ttn2 and Ttn3) titanites (Fig. 5). These differences in trace elements are strongly affected by the formation conditions, such as T, fO_2, fS_2 and composition of melt or fluid (Tiepolo et al. 2002; Cao et al. 2015; Xiao et al. 2021). Hydrothermal Ttn2 and Ttn3 show higher HFSE concentrations and Lu/Hf ratios than the magmatic Ttn1, similar to hydrothermal titanites from other regions documented by Fu et al. (2016) and Xiao et al. (2021). Enrichment of HFSE in hydrothermal titanite suggests that HFSE can be mobile in hydrothermal fluids during silicification, sericitization and carbonation. However, in contrast to other studies, the hydrothermal titanites (Ttn2 and Ttn3) have higher ΣREE compared with magmatic titanite (Ttn1). This implies that the hydrothermal fluids were relatively enriched in REE. This interpretation is also consistent with the ubiquitous presence of monazite in the quartz-pyrite veins.

Despite the differences in REE contents, the magmatic and hydrothermal titanites show similar chondrite-normalized REE patterns (Supplementary Fig. A1), which suggest that the hydrothermal fluids that precipitated Ttn2 and Ttn3 were most likely exsolved from the same monzonitic magma that crystallized Ttn1. This conclusion is further supported by the overlapping crystallization ages of magmatic Ttn1 (120.7 ± 3.1 Ma) and hydrothermal Ttn2 and Ttn3 (120.9

± 2.6 Ma), and by the indistinguishable $\varepsilon_{Nd}(t)$ values of the three titanite types (Fig. 7). The latter also implies the same Nd isotope composition of the monzonitic magma and hydrothermal fluids, further suggesting the co-genetic origin between magma and fluid.

Given its high Nd content, magmatic titanite could shed light on the Nd isotope composition of the magma (e.g., Xie et al. 2010; Cao et al., 2015). The homogeneous $\varepsilon_{Nd}(t)$ values (-14.7 to -13.0) of magmatic Ttn1 are higher than the whole-rock $\varepsilon_{Nd}(t)$ values of the lower crustal-sourced Linglong granite (-21.6 to -19.2), Gushan granite (-18.9 to -18.6) and Aishan granite (-17.9 to -16.2) (Yang et al. 2012; Li et al. 2012b; Li et al. 2019a), but within the range of the Guojialing granodiorite (-16.8 to -11.5), which has been interpreted as deriving from a mixture of mantle and lower crustal sources (Yang et al. 2012; Li et al. 2019a). Additionally, early Cretaceous mafic dikes in the Jiaodong area have $\varepsilon_{Nd}(t)$ that overlap with range of Ttn1 (-18.1 to -13.6; Cai et al. 2013) (Fig. 7). Taken as a whole, these data support a mixed mantle and lower crustal source for the monzonitic magma (Fig. 11a).

Interpretation of pyrite geochemistry

Trace elements and S isotopes of pyrite record valuable information about the source and properties (pH, redox, temperature) of the fluids from which the pyrite formed (Pokrovski et al. 2002; Deditius et al. 2014; Peterson and Mavrogenes 2014; Li et al. 2018). Four types of pyrite identified in this study have been characterized for trace elements and S isotopes, and the implications

of these results are discussed here.

The isolated Py1 grains show features consistent with a magmatic origin, including: disseminated occurrence in fresh monzonite; coexistence with magmatic magnetite, plagioclase, quartz and titanite; homogeneous BSE response; and low concentrations of trace metals (Co, Ni, Cu, Zn, As, Ag, Sb, Pb and Bi). The Py1 grains also show several similarities with Py4 grains found in the fresh mafic enclaves from the Gushan granite. The Py4 occurs as euhedral to anhedral crystals in the matrix and coexists with magnetite and allanite (Fig. 8d, h). Both Py1 and Py4 are therefore interpreted as being of magmatic origin. Both Py1 and Py4 also have broadly similar and relatively low values of $\delta^{34}S$ (+1.9 to +6.3 ‰ and +5.0 to +6.4 ‰, respectively), which represent the sulfur isotopic compositions of the magma. Previous research has suggested that the mafic enclaves from the Gushan granite were formed by mixing between mafic and felsic magmas (Li et al. 2012b), during which both chemical and isotopic compositions tend to reach homogenization. The felsic magma was sourced from the ancient NCC lower crust at ca. 120 Ma, and the mafic magma was derived from an enriched lithospheric mantle source beneath eastern NCC (Li et al. 2012b). Similarly, the above results of Nd isotopes in titanite suggest a potentially mixed mantle/lower crustal source for the monzonitic magma at ca. 121 Ma. Thus, we interpret that the sulfur isotopic compositions of Py1 and Py4 represent the products of isotopic exchange between lower crust-derived felsic magma and lithospheric mantle-derived mafic magma.

In contrast to Py1 and Py4, Py2 and Py3 show features typical of hydrothermal origin. Py2 occurs mostly as anhedral clusters in the altered monzonite, coexists with sericite, calcite, and pyrrhotite, and displays heterogeneous textures under BSE (Fig. 8f). In addition, Py2 shows variable and relatively high concentrations of minor and trace metals (especially Co, As, Ag, Sb and Bi). Significantly, extremely high contents of Au (18.7 ppm) and Bi (16.8 ppm) suggest the presence of gold as submicron inclusions in Py2. The latter implies that the hydrothermal fluids that deposited Py2 had potential for forming precious-metal mineralization. Py3 occurs in the quartz-pyrite veins, and thus is unambiguously of hydrothermal origin. Py3 shows various broad similarities with pyrite from the Jiaodong Au province, especially high As contents and $\delta^{34}S$ values of +6.5 to +7.6 ‰.

Pyrrhotite grains commonly occur as rims on or fracture fill within the Py2 grains, implying that pyrrhotite formed later than Py2. However, the pyrrhotite and Py2 display similar $\delta^{34}S$ values ($\delta^{34}S_{po}$ = +6.9 to +8.8 ‰, $\delta^{34}S_{Py2}$ = +6.4 to +9.5 ‰), which are indicative of natural sulfur isotopic fractionation between pyrite and pyrrhotite precipitated from hydrothermal fluids with the same sulfur ratios ($\delta^{34}S$) (e.g., Li et al. 2017). The precipitation of early pyrite transitioning to later pyrrhotite suggests a decrease of sulfur fugacity in the evolving hydrothermal fluid, probably due to the consumption of sulfur by pyrite, or perhaps by effervescence of H_2S.

Considering that the hydrothermal sulfides disseminated in the monzonite

566 are dominated by pyrite and pyrrhotite, isotopic fractionation between sulfide
567 pairs is negligible, thus the sulfur isotopic signature of pyrite can reasonably
568 represent the bulk sulfur isotopic composition of the hydrothermal fluid
569 (Ohmoto 1972). Sulfur isotopes of pyrite have been widely used to trace the
570 sources of fluids (e.g., Peterson and Mavrogenes 2014; Chen et al. 2015). Based
571 on the sulfur isotopic ratios of Py2 and Py3, we suggest that the corresponding
572 hydrothermal fluids have a narrow range of $\delta^{34}S$ values (+6.4 to +9.5 ‰),
573 similar to those from the Au deposits in the Jiaodong province (+6 to +10 ‰;
574 Li et al. 2018; Feng et al. 2018; Deng et al. 2020b), but slightly heavier than the
575 monzonitic magma which was represented by the $\delta^{34}S$ of Py1 (+1.9 to +6.3 ‰)
576 (Fig. 10). The textural, geochemical and geochronological observations of the
577 magmatic-hydrothermal titanite indicate a role of magmatic-hydrothermal
578 fluids that exsolved from the monzonitic magma. These magmatic-
579 hydrothermal fluids are likely to have contributed to the precipitation of Py2
580 and Py3, as well as to silicification, sericitization and carbonation of the biotite
581 monzonite. Experimental data from Fiege et al. (2014) revealed that the
582 hydrothermal fluids released by magma degassing can have heavier S isotopes
583 than the source magma (with $\delta^{34}S$ ~6.7‰ higher) when the sulfur occurs as S^{2-}
584 or H_2S. This is compatible with the slightly heavier $\delta^{34}S$ values of the
585 hydrothermal Py2 and Py3 compared to the magmatic Py1. In addition, the age
586 of hydrothermal monazite (118.2 ± 4.6 Ma) is consistent with the age of biotite
587 monzonite (120.7 ± 3.1 Ma), further implying an intimate relationship between

588 the monzonitic magma and hydrothermal fluids. In general, we propose that the
589 hydrothermal fluids that precipitated Py2 and Py3 were directly exsolved from
590 the monzonitic magma, which had previously crystallized igneous Py1 grains.

591 **Constraints on magmatism and hydrothermal processes**

592 The deposition of titanite and pyrite in the biotite monzonite clearly spans
593 the magmatic and hydrothermal stages (Fig. 11). Our results regarding the
594 occurrence and geochemistry of titanite and pyrite provide insights into the
595 melt/fluid composition, the conditions under which they formed, and the
596 magmatic-hydrothermal processes in the monzonite system.

597 Magmatic Ttn1 formed as discrete euhedral grains intergrown with K-
598 feldspar, magnetite and quartz. This assemblage indicates that the monzonitic
599 magma crystallization occurred at a relatively high oxygen fugacity and H_2O-
600 rich environment (Frost and Lindsley 1992; Piccoli et al. 2000; Xiao et al. 2021).
601 The high oxygen fugacity is supported by the negative Eu anomaly of Ttn1.
602 High oxygen fugacity and H_2O contents could lead to a preferential transfer of
603 Au into the magma from its source (Botcharnikov et al. 2011; Wang et al. 2020),
604 resulting in Au enrichment, which is reflected by two analyses of magmatic Py1
605 that showed relatively high Au contents (0.1 ppm and 0.14 ppm). Since the Nd
606 isotopes of Ttn1 and S isotopes of Py1 are proposed to be likely the result of
607 mixing between magmas from lower crust and lithospheric mantle, the Au could
608 be derived from both sources (Fig. 11a).

609 In the later hydrothermal stages, fluids were directly exsolved from the late-

stage monzonitic magma. The complex textures and geochemistry of Ttn2 and Ttn3 suggest that formation of these minerals was a dynamic process involving different hydrothermal stages (Fig. 11b). The initial hydrothermal fluid was characterized by high REE contents (especially LREE), which resulted in back-scatter bright cores of Ttn2. With further degassing, the hydrothermal fluid precipitated back-scatter gray rims of Ttn2 with moderate REE contents (e.g., Fu et al. 2016; Xiao et al. 2021), as well as Py2 with relatively high metal contents (Co, As, Ag, Au, Sb and Bi). This implies that Au, together with Co, As, Ag, Sb and Bi, were pre-enriched in the monzonitic magma and were furthermore favorably partitioned into the exsolved fluids (Pokrovski et al. 2013). In the late hydrothermal stage, the fluid became less oxidized – evidenced by the variable negative-positive Eu anomalies (Eu_N/Eu_N^* = 0.2-1.1, average 0.6) of Ttn3 – and contained lower total REE contents. The Ttn3 precipitated at this stage overgrew on the rims of Ttn2, and partly penetrated in Ttn2 (Fig. 11b). The pyrrhotite grains were likely precipitated during the late hydrothermal stages (Fig. 11b), due to the consumption of sulfur by deposition of Py2 and less oxidizing conditions. Multiple stages of hydrothermal fluid exsolution from the monzonitic magma show the same Nd and S isotopic compositions. The hydrothermal fluids led to distinct alteration in the biotite monzonite, including silicification, sericitization and carbonation. We surmise that these same fluids then migrated along faults and fractures, forming quartz-pyrite (Py3) veins in the overlying Luanjiahe granite.

A potential magmatic-hydrothermal model for the Jiaodong Au mineralization

The source(s) of ore-forming fluids and Au, the mechanism(s) for Au enrichment, and the genetic model for the Jiaodong Au deposits have long been debated (Fan et al. 2003; Zhai et al. 2004; Chen et al. 2005; Goldfarb and Santosh 2014; Zhu et al. 2015; Deng et al. 2020b). The possible sources for the ore components include (1) a crustal source from Precambrian metamorphic rocks and/or Mesozoic granite (Chen et al. 2005), (2) a subcrustal source from volatile- and Au-fertilized metasomatized mantle lithosphere (Zhu et al. 2015; Deng et al. 2020a, b), or (3) a mixed crustal plus mantle source (Zhai et al. 2004). Various models have been postulated to explain the nature of Au mineralization in different settings, including the orogenic Au deposits (Zhou et al. 2002; Goldfarb and Santosh 2014), intrusion-related Au deposits (Sillitoe and Thompson 1998; Nie et al. 2004), magmatic-hydrothermal Au deposits related to mafic dikes (Wang et al. 2020), decratonic Au deposits (Zhu et al. 2015), and "Jiaodong-type" Au deposits (Deng et al. 2015; Li et al. 2015). All these genetic models have advantages and problems, which have been reviewed by Deng et al. (2020b), and are still highly contentious. One critical factor hindering universal acceptance of a single model is the uncertainty of genetic relationship between magmatism and Au mineralization. Ultimately, this uncertainty is underpinned by the question of whether exsolution and degassing of auriferous magmatic-hydrothermal fluid took place. The information

provided by magmatic-hydrothermal titanites and pyrites in this study highlights the exsolution of auriferous hydrothermal fluids from the monzonitic magma, and thus supports a magmatic-hydrothermal model for the genesis of the Jiaodong Au province, as discussed below.

Titanite and monazite that formed from the monzonitic magma (Ttn1) and exsolved hydrothermal fluids (Ttn2, Ttn3 and monazite) yielded consistent U-Pb ages (121-118 Ma) overlapping within error with the large-scale Au mineralization age at Jiaodong (120-119 Ma; Ma et al. 2017; Li et al. 2018; Yang et al. 2018; Deng et al. 2020a; Zhang et al. 2020). Spatially, the biotite monzonite intruded at depth beneath the Linglong goldfield, and is connected with the surface and Au deposits by the Zhaoyuan-Pingdu fault which hosts hundreds of auriferous quartz veins (Fig. 2b). Hence, our results suggest that the monzonitic magmatism and its accompanying hydrothermal fluids were both temporally and spatially linked to the Au mineralization. Magmatic pyrite (Py1) from the monzonite has relatively high Au contents (up to 0.14 ppm), suggesting that the magma was fertile for Au. Hydrothermal fluids precipitating Py2 have higher Au contents, as reflected by the presence of submicron inclusions of Au and Bi in Py2, again corroborating a genetic relationship with the Au mineralization. Quantitatively, the biotite monzonite may be part of a large-scale magmatic event at ca. 121 Ma in the Jiaodong Au province, consistent with contemporaneous intermediate-felsic rocks, including the Gushan granite located ~35 km to the southwest of the drill core (120-119 Ma;

Li et al. 2012b), the widespread intermediate-mafic (130-120 Ma; Ma et al. 2017; Wang et al. 2020) and felsic dikes (123-118 Ma; Li et al. 2019b). Extensive magmatism has the potential to produce hydrothermal fluids forming giant Au deposits. Although many researchers proposed that the ore-forming fluids were sourced from the volatile-enriched metasomatized mantle lithosphere (e.g., Goldfarb and Santosh 2014; Deng et al. 2015, 2020a, b), analyses of mantle xenoliths have suggested relatively low Au contents of the metasomatized mantle lithosphere (Wang et al., 2020), casting doubt on that interpretation. Wang et al. (2020) underscored the high Au contents of hydrous magmas that were sourced from the metasomatized mantle. These findings consistently reveal a genetic relationship between biotite monzonite, which potentially involves mantle components, and Au mineralization in the Jiaodong Au province.

Previous studies have established that the Jiaodong Peninsula experienced a transition of tectonic regime from regional compression to transpression or transtension prior to peak extension since 125-120 Ma, as a far-field response to the change of subduction direction and roll-back of the paleo-Pacific Plate (Sun et al. 2007; Yang et al. 2018; Deng et al. 2020b). The mantle lithosphere under the eastern NCC at this stage had been metasomatized during Triassic and Late Jurassic to Early Cretaceous subduction events (Chen et al. 2005; Liang et al. 2019; Deng et al. 2020a, b). The extension-induced thinning of lithosphere and accompanying asthenospheric upwelling at 130-120 Ma (Zhai et al. 2004;

Li et al. 2019a; Wu et al. 2019) triggered partial melting of the metasomatized mantle lithosphere and the lower crust of the NCC, producing hydrous mafic and felsic magmas, respectively (Fig. 11a). These magmas probably extracted Au efficiently from their sources (Wang et al. 2020). Distinct degrees of mixing occurred between the mafic and felsic magmas, forming the biotite monzonite and Gushan granite (Fig. 11a), with distinct ranges of $\varepsilon_{Nd}(t)$, which likely represent two different intrusives formed by the same magmatism. Attributing to the more involved mafic magmas, higher $\varepsilon_{Nd}(t)$ values were yielded in the biotite monzonite than the Gushan granite. With further magmatic evolution, hydrothermal fluids were exsolved from these crystallizing magmas (Fig. 11a), preferentially concentrating Au, As, Sb, Bi, S, Cl and C into the fluids by a factor of hundreds (Pokrovski et al. 2013). The auriferous fluids ascended along the translithospheric faults into second-order fault systems, and precipitated gold, quartz and sulfides. This model favors a magmatic-hydrothermal origin, and explains the intimate spatial and temporal association of Au deposits with mafic-felsic magmatism.

IMPLICATIONS

The biotite monzonite buried in the Linglong goldfield formed at ca. 121 Ma based on titanite U-Pb dating, and displays distinctive petrographic features indicative of hydrothermal alteration and mineralization, containing ubiquitous magmatic-hydrothermal titanite and pyrite. Three types of titanite with different textures and geochemistry were identified, including magmatic Ttn1 with

720 oscillatory and sector zoning under BSE, and hydrothermal Ttn2 and Ttn3
721 which show core-rim or irregular textures, and higher Fe, Mn, REE, HFSE, but
722 lower Ti, Ca contents than Ttn1. Hydrothermal fluids that precipitated Ttn2 and
723 Ttn3 were sourced from the monzonitic melt that crystallized Ttn1, evidenced
724 by similar chondrite-normalized REE patterns, indistinguishable Nd isotopes
725 ($\varepsilon_{Nd}(t)$ = -14.7 to -12.9) and U-Pb ages (120.7 ± 3.1 Ma for Ttn1, 120.9 ± 2.6
726 Ma for Ttn2 and Ttn3).

727 Four types of pyrite were analyzed, including magmatic Py1 from the fresh
728 biotite monzonite, hydrothermal Py2 from the altered biotite monzonite,
729 hydrothermal Py3 from the quartz-pyrite veins, and magmatic Py4 from the
730 mafic enclaves of the Gushan granite. The Py1 and Py4 have low concentrations
731 of trace metals, while the Py2 and Py3 have high Co, As, Ag, Au, Sb and Bi
732 contents which corresponds to fertile hydrothermal fluids. Magmatic Py1 has
733 broadly similar $\delta^{34}S$ values (+1.9 to +6.3 ‰) to Py4 (+5.0 to +6.4 ‰), but
734 relatively lighter than hydrothermal Py2 and Py3 (+6.4 to +9.5 ‰), consistent
735 with sulfur isotopic fractionation between melt and fluid. U-Pb dating of
736 monazite (118.2 ± 4.6 Ma) from the quartz-pyrite veins indicate that the
737 auriferous hydrothermal fluids are synchronous to the monzonitic magma.

738 In this contribution, evidences from the titanite and pyrite corroborate the
739 exsolution of fertile hydrothermal fluids from the monzonitic magma,
740 suggesting a magmatic-hydrothermal genetic model for the giant Jiaodong Au
741 mineralization. We infer that primary Au was efficiently extracted from the

742 metasomatized mantle lithosphere and the lower crust of the NCC by hydrous
743 magmas at ca. 120 Ma.

744 **ACKNOWLEGMENTS AND FUNDING**

745 We thank Dapeng Li and Guijun Wen for their helps during fieldworks,
746 Lihui Jia, Jiakang Kong and Zheng Liu for their technical supports in running
747 the EPMA, LA-ICPMS and LA-MC-ICPMS analyses. We are grateful to two
748 anonymous reviewers for their constructive feedback that helped to improve an
749 earlier manuscript, and associate editor Paul Tomascak for valuable suggestions
750 and efficient editorial handling. This work is funded by the National Key
751 Research and Development Program (No. 2016YFC0600105), China National
752 Postdoctoral Program for Innovative Talents (No. BX20190327), and China
753 Postdoctoral Science Foundation (No. 2019M660788).

754

REFERENCES CITED

Aleinikoff, J.N., Wintsch, R.P., Fanning, C.M., and Dorais, M.J. (2002) U-Pb geochronology of zircon and polygenetic titanite from the Glastonbury Complex, Connecticut, USA: an integrated SEM, EMPA, TIMS, and SHRIMP study. Chemical Geology, 188, 125–147.

Aleinikoff, J.N., Schenck, W.S., Plank, M.O., Srogi, L., Fanning, C.M., Kamo, S.L., and Bosbyshell, H. (2006) Deciphering igneous and metamorphic events in highgrade rocks of the Wilmington Complex, Delaware: Morphology, cathodoluminescence and backscattered electron zoning, and SHRIMP U-Pb geochronology of zircon and monazite. Geological Society of America Bulletin, 118, 39–64.

Botcharnikov, R.E., Linnen, R.L., Wilke, M., Holtz, F., Jugo, P.J., and Berndt, J. (2011) High gold concentrations in sulphide-bearing magma under oxidizing conditions. Nature Geoscience, 4, 112–115.

Bouvier, A., Vervoort, J.D., and Patchett, P.J. (2008) The Lu–Hf and Sm–Nd isotopic composition of CHUR: Constraints from unequilibrated chondrites and implications for the bulk composition of terrestrial planets. Earth and Planetary Science Letters, 273, 48–57.

Cai, Y.C., Fan, H.R., Santosh, M., Liu, X., Hu, F.F., Yang, K.F., Lan, T.G., Yang, Y.H., and Liu, Y.S. (2013) Evolution of the lithospheric mantle beneath the southeastern North China Craton: constraints from mafic dikes in the Jiaobei terrain. Gondwana Research, 24, 601–621.

777 Cao, M.J., Qin, K.Z., Li, G.M., Evans, N.J., and Jin, L.Y. (2015) In situ LA-
778 (MC)-ICP- MS trace element and Nd isotopic compositions and genesis of
779 polygenetic titanite from the Baogutu reduced porphyry Cu deposit,
780 Western Junggar, NW China. Ore Geology Reviews, 65, 940–954.
781 Chen, L., Li, X.H., Li, J.W., Hofstra, A.H., Liu, Y., and Koenig, A.E. (2015)
782 Extreme variation of sulfur isotopic compositions in pyrite from the
783 Qiuling sediment-hosted gold deposit, West Qinling orogen, central China:
784 an *in situ* SIMS study with implications for the source of sulfur.
785 Mineralium Deposita, 50, 643–656.
786 Chen, Y.J., Pirajno, F., and Qi, J.P. (2005) Origin of gold metallogeny and
787 sources of ore-forming fluids, Jiaodong Province, Eastern China.
788 International Geology Review, 47, 530–549.
789 Dare, S.A.S., Barnes, S.J., Beaudoin, G., Méric, J., Boutroy, E., and Potvin-
790 Doucet, C. (2014) Trace elements in magnetite as petrogenetic indicators.
791 Mineralium Deposita, 49, 785–796.
792 Deditius, A.P., Reich, M., Kesler, S.E., Utsunomiya, S., Chryssoulis, S.L.,
793 Walshe, J., and Ewing, R.C. (2014) The coupled geochemistry of Au and
794 As in pyrite from hydrothermal ore deposits. Geochimica et
795 Cosmochimica Acta, 140, 644–670.
796 Deng, J., Wang, C., Bagas, L., Carranza, E.J.M., and Lu, Y. (2015) Cretaceous–
797 Cenozoic tectonic history of the Jiaojia Fault and gold mineralization in
798 the Jiaodong Peninsula, China: constraints from zircon U-Pb, illite K-Ar,

799 and apatite fission track thermochronometry. Mineralium Deposita, 50,
800 987–1006.
801 Deng, J., Qiu, K.F., Wang, Q.F., Goldfarb, R.J., Yang, L.Q., Zi, J.W., Geng, J.Z.,
802 and Ma, Y. (2020a) In-situ dating of hydrothermal monazite and
803 implications on the geodynamic controls of ore formation in the Jiaodong
804 gold province, eastern China. Economic Geology, 115, 671–685.
805 Deng, J., Yang, L.Q., Groves, D.I., Zhang, L., Qiu, K.F., and Wang, Q.F. (2020b)
806 An integrated mineral system model for the gold deposits of the giant
807 Jiaodong province, eastern China. Earth-Science Reviews, 208, 103274.
808 Dora, M.L., Upadhyay, D., Randive, K.R., Shareef, M., Baswani, S.R., and
809 Ranjan, S. (2020) Trace element geochemistry of magnetite and pyrite and
810 sulfur isotope geochemistry of pyrite and barite from the Thanewasna Cu-
811 (Au) deposit, western Bastar Craton, central India: Implication for ore
812 genesis. Ore Geology Reviews, 117, 103262.
813 Fan, H.R., Zhai, M.G., Xie, Y.H., and Yang, J.H. (2003) Ore-forming fluids
814 associated with granite-hosted gold mineralization at the Sanshandao
815 deposit, Jiaodong gold province, China. Mineralium Deposita, 38, 739–
816 750.
817 Fan, H.R., Hu, F.F., Yang, J.H., and Zhai, M.G. (2007) Fluid evolution and
818 large-scale gold metallogeny during Mesozoic tectonic transition in the
819 Jiaodong Peninsula, eastern China. Geological Society London Special
820 Publications, 280, 303–316.

821 Feng, K., Fan, H.R., Hu, F.F., Yang, K.F., Liu, X., Shangguan, Y.N., and Jiang,
822 P. (2018) Involvement of anomalously As-Au-rich fluids in the
823 mineralization of the Heilan'gou gold deposit, Jiaodong, China: evidence
824 from trace element mapping and in-situ sulfur isotope composition.
825 Journal of Asian Earth Sciences, 160, 304–321.
826 Feng, K., Fan, H.R., Groves, D.I., Yang, K.F., Hu, F.F., Liu, X., and Cai, Y.C.
827 (2020) Geochronological and sulfur isotopic evidence for the genesis of
828 the post-magmatic, deeply sourced, and anomalously gold-rich Daliuhang
829 orogenic deposit, Jiaodong, China. Mineralium Deposita, 55, 293–308.
830 Fiege, A., Holtz, F., Shimizu, N., Mandeville, C.W., Behrens, H., and Knipping,
831 J.L. (2014) Sulfur isotope fractionation between fluid and andesitic melt:
832 An experimental study. Geochimica et Cosmochimica Acta, 142, 501–521.
833 Frost, B.R., and Lindsley, D.H. (1992) Equilibria among Fe-Ti oxides,
834 pyroxenes, olivine, and quartz: part II. Application. American Mineralogist,
835 77, 1004–1020.
836 Frost, B.R., Chamberlain, K.R., and Schumacher, J.C. (2001) Sphene (titanite):
837 phase relations and role as a geochronometer. Chemical Geology, 172,
838 131–148.
839 Fu, J.L., Hu, Z.C., Zhang, W., Yang, L., Liu, Y.S., Li, M., Zong, K.Q., Gao, S.,
840 and Hu, S.H. (2016) In situ, sulfur isotopes ($\delta^{34}S$ and $\delta^{33}S$) analyses in
841 sulfides and elemental sulfur using high sensitivity cones combined with
842 the addition of nitrogen by Laser Ablation MC-ICP-MS. Analytica

Chimica Acta, 911, 14–26.

Gilbert, S.E., Danyushevsky, L.V., Rodemann, T., Shimizu, N., Gurenko, A., Meffre, S., Thomas, H., Large, R.R., and Death, D. (2014) Optimisation of laser parameters for the analysis of sulphur isotopes in sulphide minerals by laser ablation ICP-MS. Journal of Analytical Atomic Spectrometry, 29, 1042–1051.

Goldfarb, R.J., and Santosh, M. (2014) The dilemma of the Jiaodong gold deposits: Are they unique? Geoscience Frontiers, 5, 139–153.

Goss, S.C., Wilde, S.A., Wu, F.Y., and Yang, J.H. (2010) The age, isotopic signature and significance of the youngest Mesozoic granitoids in the Jiaodong Terrain, Shandong Province, North China Craton. Lithos, 120, 309–326.

Groves, D.I., Goldfarb, R.J., Gebre-Mariam, M., Hagemann, S.G., and Robert, F. (1998) Orogenic gold deposits: a proposed classification in the context of their crustal distribution and relationship to other gold deposit types. Ore Geology Reviews, 13, 7–27.

Hamilton, P.J., O'Nions, R.K., Bridgwater, D., and Nutman, A. (1983) Sm-Nd studies of Archaean metasediments and metavolcanics from West Greenland and their implications for the Earth's early history. Earth and Planetary Science Letters, 62, 263–272.

Hayden, L.A., Watson, E.B., Wark, D.A. (2008) A thermobarometer for sphene (titanite). Contributions to Mineralogy and Petrology, 155, 529–540.

865 Hu, Z.C., Zhang, W., Liu, Y.S., Gao, S., Li, M., Zong, K.Q., Chen, H.H., and
866 Hu, S.H. (2015) "Wave" signal-smoothing and mercury-removing device
867 for laser ablation quadrupole and multiple collector ICPMS analysis:
868 application to lead isotope analysis. Analytical Chemistry, 87, 1152–1157.
869 Jacobsen, S.B., and Wasserburg, G.J. (1980) Sm-Nd isotopic evolution of
870 chondrites. Earth and Planetary Science Letters, 50, 139–155.
871 Li, J., Xu, L.L., Bi, X.W., Tang, Y.Y., Sheng, X.Y., Yu, H.J., Liu, G., and Ma, R.
872 (2020) New titanite U–Pb and molybdenite Re–Os ages for a hydrothermal
873 vein-type Cu deposit in the Lanping Basin, Yunnan, SW China: constraints
874 on regional metallogeny and implications for exploration. Mineralium
875 Deposita. https://doi.org/10.1007/s00126-020-00973-x.
876 Li, J.W., Deng, X.D., Zhou, M.F., Liu, Y.S., Zhao, X.F., and Guo, J.L. (2010)
877 Laser ablation ICP–MS titanite U–Th–Pb dating of hydrothermal ore
878 deposits: a case study of the Tonglushan Cu–Fe–Au skarn deposit, SE
879 Hubei Province, China. Chemical Geology, 270, 56–67.
880 Li, J.W., Bi, S.J., Selby, D., Chen, L., Vasconcelos, P., Thiede, D., Zhou, M.F.,
881 Zhao, X.F., Li, Z.K., and Qiu, H.N. (2012a) Giant Mesozoic gold
882 provinces related to the destruction of the North China craton. Earth and
883 Planetary Science Letters, 349, 26–37.
884 Li, L., Santosh, M., and Li, S.R. (2015) The 'Jiaodong type' gold deposits:
885 characteristics, origin and prospecting. Ore Geology Reviews, 65, 589–
886 611.

887 Li, R.C., Chen, H.Y., Xia, X.P., Yang, Q., Li, L., Xu, J., Huang, C., and
888 Danyushevsky, L.V. (2017) Ore fluid evolution in the giant Marcona Fe-
889 (Cu) deposit, Perú: Evidence from in-situ sulfur isotope and trace element
890 geochemistry of sulfides. Ore Geology Reviews, 86, 624–638.
891 Li, X.C., Fan, H.R., Santosh, M., Hu, F.F., Yang, K.F., Lan, T.G., Liu, Y., and
892 Yang, Y.H. (2012b) An evolving magma chamber within extending
893 lithosphere: an integrated geochemical, isotopic and zircon U–Pb
894 geochronological study of the Gushan granite, eastern North China Craton.
895 Journal of Asian Earth Sciences, 50, 27–43.
896 Li, X.H., Fan, H.R., Yang, K.F., Hollings, P., Liu, X., Hu, F.F., and Cai, Y.C.
897 (2018) Pyrite textures and compositions from the Zhuangzi Au deposit,
898 southeastern North China craton: Implication for ore-forming processes.
899 Contributions to Mineralogy and Petrology, 73, 73.
900 Li, X.H., Fan, H.R., Hu, F.F., Hollings, P., Yang, K.F., and Liu, X. (2019a)
901 Linking lithospheric thinning and magmatic evolution of late Jurassic to
902 early cretaceous granitoids in the Jiaobei Terrane, southeastern North
903 China Craton. Lithos, 324, 280–296.
904 Li, X.H., Fan, H.R., Santosh, M., Yang, K.F., Peng, H.W., Hollings, P., and Hu,
905 F.F. (2019b) Mesozoic felsic dikes in the Jiaobei Terrane, southeastern
906 North China Craton: Constraints from zircon geochronology and
907 geochemistry, and implications for gold metallogeny. Journal of
908 Geochemical Exploration, 201, 40–55.

909 Liang, Y.Y., Deng, J., Liu, X., Wang, Q., Ma, Y., Gao, T., Zhao, L. (2019) Water
910 contents of Early Cretaceous mafic dikes in the Jiaodong Peninsula,
911 eastern North China Craton: insights into an enriched lithospheric mantle
912 source metasomatized by paleo–Pacific Plate subduction–related fluids.
913 The Journal of Geology, 127, 343–362.
914 Liu, S., Hu, R.Z., Gao, S., Feng, C.X., Yu, B.B., Qi, Y.Q., Wang, T., Feng, G.Y.,
915 and Coulson, I.M. (2009) Zircon U-Pb age, geochemistry and Sr–Nd–Pb
916 isotopic compositions of adakitic volcanic rocks from Jiaodong, Shandong
917 Province, Eastern China: constraints on petrogenesis and implications.
918 Journal of Asian Earth Sciences, 35, 445–458.
919 Liu, Y.S., Hu, Z.C., Gao, S., Günther, D., Xu, J., Gao, C.G., and Chen, H.H.
920 (2008) In situ analysis of major and trace elements of anhydrous minerals
921 by LA-ICP-MS without applying an internal standard. Chemical Geology,
922 257, 34–43.
923 Ludwig, K.R. (2003) ISOPLOT 3.00: A Geochronological Toolkit for Microsoft
924 Excel. Berkeley Geochronology Center, California, Berkeley, pp 39.
925 Ma, W.D., Fan, H.R., Liu, X., Pirajno, F., Hu, F.F., Yang, K.F., Yang, Y.H., Xu,
926 W.G., and Jiang, P. (2017) Geochronological framework of the Xiadian
927 gold deposit in the Jiaodong province, China: implications for the timing
928 of gold mineralization. Ore Geology Reviews, 86, 196–211.
929 Mao, J.W., Wang, Y.T., Li, H.M., Pirajno, F., Zhang, C.Q., and Wang, R.T. (2008)
930 The relationship of mantle-derived fluids to gold metallogenesis in the

931 Jiaodong Peninsula: evidence from D-O-C-S isotope systematics. Ore
932 Geology Reviews, 33, 361–381.
933 Miao, L.C., Luo, Z.K., Huang, J.Z., Guan, K., Wang, L.G., McNaughton, N.J.,
934 and Groves, D.I. (1997) Zircon Sensitive High Resolution Ion Microprobe
935 (SHRIMP) study of granitoid intrusions in Zhaoye Gold Belt of Shandong
936 Province and its implication. Science in China (Series D), 40, 361–369.
937 Mills, S.E., Tomkins, A.G., Weinberg, R.F., and Fan, H.R. (2015) Implications
938 of pyrite geochemistry for gold mineralisation and remobilisation in the
939 Jiaodong gold district, northeast China. Ore Geology Reviews, 71, 150–
940 168.
941 Morad, S., El-Ghali, M.A.K., Caja, M.A., Al-Ramadan, K., and Mansurbeg, H.
942 (2009) Hydrothermal alteration of magmatic titanite: evidence from
943 Proterozoic granitic rocks, Southeastern Sweden. Canadian Mineralogist,
944 47, 801–811.
945 Nie, F.J., Jiang, S.H., and Liu, Y. (2004) Intrusion-related gold deposits of North
946 China Craton, People's Republic of China. Resource Geology, 54, 299–
947 324.
948 Ohmoto, H. (1972) Systematics of sulfur and carbon isotopes in hydrothermal
949 ore deposits. Economic Geology, 67, 551–578.
950 Olin, P.H., and Wolff, J.A. (2012) Partitioning of rare earth and high field
951 strength elements between titanite and phonolitic liquid. Lithos, 128–131,
952 46–54.

953 Peterson, E., and Mavrogenes, J. (2014) Linking high-grade gold mineralization
954 to earthquake-induced fault-valve processes in the Porgera gold deposit,
955 Papua New Guinea. Geology, 42, 383–386.
956 Piccoli, P., Candela, P., and Rivers, M. (2000) Interpreting magmatic processes
957 from accessory phases: titanite–a small-scale recorder of large-scale
958 processes. Transactions of the Royal Society of Edinburgh Earth Sciences,
959 91, 257–267.
960 Pokrovski, G.S., Kara, S., and Roux, J. (2002) Stability and solubility of
961 arsenopyrite, FeAsS, in crustal fluids. Geochimica et Cosmochimica Acta,
962 66, 2361–2378.
963 Pokrovski, G.S., Borisova, A.Y., and Bychkov, A.Y. (2013) Speciation and
964 transport of metals and metalloids in geological vapors: Reviews in
965 Mineralogy and Geochemistry, 76, 165–218.
966 Qiu, Y.M., Groves, D.I., McNaughton, R.J., and Phillips, G.N. (2002) Nature,
967 age, and tectonic setting of granitoid-hosted, orogenic gold deposits of the
968 Jiaodong Peninsula, eastern North China Craton, China. Mineraliun
969 Deposita, 37, 283–305.
970 Shen, Y.K., Guo, T., Yang, Y.Q., Chen, Z.L., Wei, C.S., and Sun, H.S. (2016)
971 Discovery of biotite monzonite and Ar-Ar thermochronology significance
972 in Linglong gold field. Journal of Geomechanics, 22, 778–793 (in Chinese
973 with English abstract).
974 Sillitoe, R.H., and Thompson, J.F. (1998) Intrusion–related vein gold deposits:

types, tectono-magmatic settings and difficulties of distinction from orogenic gold deposits. Resource Geology, 48, 237–250.

Spandler, C., Hammerli, J., Sha, P., Hilbert-Wolf, H., Hu, Y., Roberts, E., and Schmitz, M. (2016) MKED1: A new titanite standard for in situ analysis of Sm–Nd isotopes and U–Pb geochronology. Chemical Geology, 425, 110–126.

Sun, W.D., Ding, X., Hu, Y.H., and Li, X.H. (2007) The golden transformation of the Cretaceous plate subduction in the west Pacific. Earth and Planetary Science Letters, 262, 533–542.

Tanner, D., Henley, R.W., Mavrogenes, J.A., and Holden, P. (2016) Sulfur isotope and trace element systematics of zoned pyrite crystals from the El Indio Au–Cu–Ag deposit, Chile. Contributions to Mineralogy and Petrology, 171, 33.

Tiepolo, M., Oberti, R., and Vannucci, R. (2002) Trace-element incorporation in titanite: constraints from experimentally determined solid/liquid partition coefficients. Chemical Geology, 191, 105–119.

Wang, Z.C., Cheng, H., Zong, K.Q., Geng, X.L., Liu, Y.S., Yang, J.H., Wu, F.Y., Becker, H., Foley, S., and Wang, C.Y. (2020) Metasomatized lithospheric mantle for Mesozoic giant gold deposits in the North China craton. Geology, 48, 169–173.

Wen, B.J., Fan, H.R., Santosh, M., Hu, F.F., Pirajno, F., Yang, K.F. (2015) Genesis of two different types of gold mineralization in the Linglong gold

997 field, China: constrains from geology, fluid inclusions and stable isotope.
998 Ore Geology Reviews, 65, 643–658.
999 Wiedenbeck, M., Alle, P., Corfu, F., Griffin, W.L., Meier, M., Oberli, F., Quadt,
1000 A.V., Roddick, J.C., and Spiegel, W. (1995) Three natural zircon standards
1001 for U–Th–Pb, Lu–Hf, trace element and REE analyses. Geostandards and
1002 Geoanalytical Research, 19, 1–23.
1003 Wu, F.Y., Yang, J.H., Xu, Y.G., Wilde, S.A., and Walker, R.J. (2019) Destruction
1004 of the North China craton in the Mesozoic. Annual Review of Earth and
1005 Planetary Sciences, 47, 173–195.
1006 Xiao, X., Zhou, T.F., White, N.C., Zhang, L.J., Fan, Y., and Chen, X.F. (2021)
1007 Multiple generations of titanites and their geochemical characteristics
1008 record the magmatic-hydrothermal processes and timing of the
1009 Dongguashan porphyry-skarn Cu-Au system, Tongling district, Eastern
1010 China. Mineralium Deposita, 56, 363–380.
1011 Xie, L., Wang, R.C., Chen, J., and Zhu, J.C. (2010) Mineralogical evidence for
1012 magmatic and hydrothermal processes in the Qitianling oxidized tin
1013 bearing granite (Hunan, South China): EMP and (MC)-LA-ICPMS
1014 investigations of three types of titanite. Chemical Geology, 276, 53–68.
1015 Xie, S.W., Wu, Y.B., Zhang, Z.M., Qin, Y.C., Liu, X.C., Wang, H., Qin, Z.W.,
1016 Liu, Q., and Yang, S.H. (2012) U-Pb ages and trace elements of detrital
1017 zircons from Early Cretaceous sedimentary rocks in the Jiaolai Basin,
1018 north margin of the Sulu UHP terrain: provenances and tectonic

implications. Lithos, 154, 346–360.

Xu, H.J., Zhang, J.F., Wang, Y.F., and Liu, W.L. (2016) Late triassic alkaline complex in the Sulu UHP terrane: implications for post-collisional magmatism and subsequent fractional crystallization. Gondwana Research, 35, 390–410.

Xu, L., Hu, Z., Zhang, W., Yang, L., Liu, Y., Gao, S., Luo, T., and Hu, S. (2015) In situ Nd isotope analyses in geological materials with signal enhancement and non-linear mass dependent fractionation reduction using laser ablation MC-ICP-MS. Journal of Analytical Atomic Spectrometry, 30, 232–244.

Yang, J.H., and Zhou, X.H. (2001) Rb-Sr, Sm-Nd, and Pb isotope systematics of pyrite: Implications for the age and genesis of lode gold deposits. Geology, 29, 711–714.

Yang, K.F., Fan, H.R., Santosh, M., Hu, F.F., Wilde, S.A., Lan, T.G., Lu, L.N., and Liu, Y.S. (2012) Reactivation of the Archean lower crust: implications for zircon geochronology, elemental and Sr-Nd-Hf isotopic geochemistry of late Mesozoic granitoids from northwestern Jiaodong Terrain, the North China Craton. Lithos, 146, 112–127.

Yang, K.F., Jiang, P., Fan, H.R., Zuo, Y.B., and Yang, Y.H. (2018) Tectonic transition from a compressional to extensional metallogenic environment at ~120 Ma revealed in the Hushan gold deposit, Jiaodong, North China Craton. Journal of Asian Earth Sciences, 160, 408–425.

1041 Zhai, M.G., Fan, H.R., Yang, J.H., and Miao, L.C. (2004) Large-scale cluster of
1042 gold deposits in east Shandong: anorogenic metallogenesis. Earth Science
1043 Frontiers, 11, 85–98 (in Chinese with English abstract).
1044 Zhang, L., Weinberg, R.F., Yang, L.Q., Groves, D.I., Sai, S.X., Matchan, E.,
1045 Phillips, D., Kohn, B.P., Miggins, D.P., Liu, Y., and Deng, J. (2020)
1046 Mesozoic orogenic gold mineralization in the Jiaodong Peninsula, China:
1047 a focused event at 120 ± 2 Ma during cooling of pre-gold granite intrusions.
1048 Economic Geology, 115, 415–441.
1049 Zheng, Y.F. (2008) A perspective view on ultrahigh-pressure metamor- phism
1050 and continental collision in the Dabie–Sulu orogenic belt. Chinese Science
1051 Bulletin, 53, 3081–3104.
1052 Zhi, Z.Y., Li, L., Li, S.R., Santosh, M., Yuan, M.W., and Alam, M. (2019)
1053 Magnetite as an indicator of granite fertility and gold mineralization: A
1054 case study from the Xiaoqinling gold province, North China Craton. Ore
1055 Geology Reviews, 115, 103159.
1056 Zhou, J.B., Wilde, S.A., Zhao, G.C., Zhang, X.Z., Zheng, C.Q., Jin, W., and
1057 Cheng, H. (2008) SHRIMP U–Pb zircon dating of the Wulian complex:
1058 defining the boundary between the North and South China Cratons in the
1059 Sulu Orogenic Belt, China. Precambrian Research, 162, 559–576.
1060 Zhou, T.H., Goldfarb, R.J., and Phillips, G.N. (2002) Tectonics and distribution
1061 of gold deposits in China: an overview. Mineralium Deposita, 37, 249–282.
1062 Zhu, R.X., Fan, H.R., Li, J.W., Meng, Q.R., Li, S.R., and Zeng, Q.D. (2015)

1063 Decratonic gold deposits. Science China Earth Sciences, 58, 1523–1537.

1064

Figure captions

Fig. 1 Geological map showing the distribution of basement rocks, UHP metamorphic rocks, Mesozoic igneous rocks and Au deposits in the three Au belts of the Jiaodong Au province. Modified after Yang et al. (2012).

Fig. 2 (**a**) Geologic map of the Linglong goldfield, showing the distribution of the orebodies, modified after Wen et al. (2015). (**b**) Cross-section of the Line 72 in the Linglong goldfield and sample location.

Fig. 3 Photographs of hand specimen and thin section cross-polarized illumination of biotite monzonite, containing disseminated pyrite. (**a, c**) Fresh-weakly altered biotite monzonite. (**b, d**) Silicified-sericitized biotite monzonite. (**e**) Quartz-pyrite veins in Luanjiahe granite. (**f**) Mafic enclave in Gushan granite. (**g, h**) Photomicrographs of biotite monzonite. *Qtz* quartz, *Kfs* k-feldspar, *Pl* plagioclase, *Bt* biotite, *Cal* calcite, *Py* pyrite.

Fig. 4 BSE images of three types of titanite and monazite. (**a, b**) Ttn1 with euhedral-subhedral shape and oscillatory zones. (**c-e**) Ttn2 with euhedral-subhedral shape and core-rim texture, coexisting with pyrite and pyrrhotite. (**f-h**) Dark-grey BSE Ttn3 penetrating and/or overgrowing Ttn2 and coexisting with calcite. (**i**) Hydrothermal monazite for U-Pb dating, from quartz-sulfide veins. Red circles show the location of points for LA-ICPMS U-Pb dating, together with ^{207}Pb-corrected $^{206}Pb/^{238}U$ ages. *Ttn* titanite, *Py* pyrite, *Po* pyrrhotite, *Mt* magnetite, *Cal* calcite, *Bt* biotite, *Qtz* quartz, *Mnz* monazite, *Rt* rutile.

Fig. 5 Selected binary plots showing the geochemical characteristics of three types of titanite. Plots of (**a**) TiO_2 versus FeO, (**b**) TiO_2 versus MnO, (**c**) CaO versus REE, (**d**) CaO versus LREE/HREE, (**e**) Eu_N/Eu_N* versus Lu/Hf, (**f**) Th versus Pb.

Fig. 6 Tera-Wasserburg diagrams and corresponding weighted mean plots of age data for (**a**) magmatic titanite (Ttn1), (**b**) hydrothermal titanite (Ttn2, Ttn3) from the biotite monzonite, and (**c**) hydrothermal monazite from the quartz-pyrite veins.

Fig. 7 $\varepsilon_{Nd}(t)$ values of titanite from the biotite monzonite, and comparison with whole-rock $\varepsilon_{Nd}(t)$ values of Mesozoic magmatic rocks in the Jiaodong Peninsula. Data are from Li et al. (2012); Yang et al. (2012); Cai et al. (2013); Li et al. (2019); and this study.

Fig. 8 Reflected light photomicrographs and BSE images of four types of pyrite. (**a, e**) Py1 with homogeneous texture under BSE is from the fresh to weakly altered biotite monzonite, coexisting with magnetite, enclosing magmatic titanite and plagioclase. (**b, f**) Py2 occurs with pyrrhotite and shows heterogeneous texture under BSE, from silicified-sericitized biotite monzonite. (**c, g**) Py3 is from the quartz-pyrite veins, showing systematic zones. (**d, h**) Py4 is from the mafic enclave in the Gushan granite, occurring with magnetite, chalcopyrite and allanite. *Py* pyrite, *Po* pyrrhotite, *Mt* magnetite, *Ccp* chalcopyrite, *Ttn* titanite, *Pl* plagioclase, *Mnz* monazite, *Aln* allanite.

Fig. 9 Trace elements of four types of pyrite. Note that some data with a value of 0 are not plotted on the diagram, and the contents of Sb and Au for Py4 are below the detection limit.

Fig. 10 *In situ* sulfur isotopes of four types of pyrite and pyrrhotite. The $\delta^{34}S$ peak of pyrite from the Jiaodong Au province is from Mao et al. (2008), Feng et al. (2018), Li et al. (2018), and Deng et al. (2020b).

Fig. 11 Schematic diagram showing (**a**) the formation of the biotite monzonite, and the contribution of magmatic-hydrothermal fluids to Au deposits in the Jiaobei Terrane; (**b**) titanite and pyrite fingerprint of hydrothermal fluids exsolved from the monzonitic magma. The monzonite formed by partial melting of the lower crust of the NCC with involvement of mantle materials at ca. 120 Ma, probably leading to preconcentration of Au, releasing auriferous magmatic-hydrothermal fluids at late stage.

Table Captions

Table 1 Results of *in situ* LA-ICPMS U-Pb dating on titanite and monazite

Electronic Supplementary materials

Supplementary Table 1 *In situ* major, trace elements and Nd isotopes of magmatic and hydrothermal titanite

Supplementary Table 2 *In situ* trace elements and/or sulfur isotopes of pyrite, pyrrhotite and magnetite

Supplementary Figures Including **Fig. A1** Chondrite-normalized REE distribution patterns for three types of titanite from the biotite monzonite; **Fig. A2** Discrimination of magnetite from the monzonite based on Ti vs. Ni/Cr, after Dare et al. (2014)

Table 1 Results of in-situ LA-ICPMS U-Pb dating on titanite and monazite

Spot No.	Isotopic ratios							^{207}Pb-corr. Age/Ma	
	^{207}Pb/^{206}Pb	1σ	^{207}Pb/^{235}U	1σ	^{206}Pb/^{238}U	1σ	rho	^{206}Pb/^{238}U	1σ
Magmatic Ttn1									
1	0.1598	0.0208	0.3634	0.0221	0.0211	0.0008	0.61	116.1	4.9
2	0.2606	0.0235	0.6647	0.0403	0.0234	0.0009	0.65	110.1	5.8
3	0.1633	0.0274	0.6964	0.0738	0.0234	0.0019	0.75	128.3	11.8
4	0.0729	0.0044	0.1717	0.0086	0.0182	0.0005	0.50	112.7	2.9
5	0.2633	0.0319	0.6636	0.0451	0.0243	0.0014	0.86	113.7	8.9
6	0.0766	0.0048	0.1939	0.0102	0.0192	0.0004	0.42	118.5	2.7
7	0.1197	0.0086	0.3036	0.0164	0.0208	0.0006	0.54	120.9	3.9
8	0.0627	0.0024	0.1663	0.0058	0.0195	0.0003	0.44	122.4	1.9
9	0.0921	0.0056	0.2367	0.0107	0.0197	0.0004	0.47	119.1	2.7
10	0.2415	0.0223	0.7310	0.0459	0.0243	0.0012	0.77	117.7	7.4
11	0.1194	0.0243	1.1518	0.1443	0.0287	0.0027	0.76	166.9	17.1
12	0.0866	0.0265	7.4754	1.3708	0.0813	0.0131	0.88	485.7	78.0
13	0.4009	0.0605	33.8111	3.6589	0.2907	0.0282	0.89	1002.1	140.6
14	0.2696	0.0315	6.4758	0.4805	0.0707	0.0051	0.98	323.7	30.9
15	0.2094	0.0407	4.5784	0.6724	0.0599	0.0062	0.70	303.0	37.5
16	0.2757	0.0431	16.8791	1.9652	0.1484	0.0133	0.77	662.4	74.4
17	0.1520	0.0297	2.6638	0.2484	0.0382	0.0033	0.92	211.3	20.4
18	0.3438	0.0383	4.1160	0.2788	0.0578	0.0037	0.95	232.0	22.6
Hydrothermal Ttn2 and Ttn3									
1	0.2123	0.0221	0.4920	0.0286	0.0224	0.0010	0.79	114.0	6.5
2	0.2795	0.0168	0.8772	0.0412	0.0249	0.0008	0.68	113.5	5.0
3	0.1340	0.0066	0.3677	0.0143	0.0208	0.0005	0.58	118.8	2.9
4	0.1493	0.0062	0.4139	0.0138	0.0208	0.0004	0.60	116.1	2.6
5	0.3672	0.0403	1.6644	0.1172	0.0315	0.0019	0.86	121.6	12.0
6	0.3558	0.0225	1.1918	0.0577	0.0279	0.0012	0.86	110.0	7.3
7	0.4104	0.0244	1.7262	0.0935	0.0328	0.0011	0.60	115.3	6.7
8	0.1584	0.0059	0.4712	0.0157	0.0220	0.0005	0.66	121.2	3.0
9	0.2281	0.0108	0.7052	0.0224	0.0243	0.0006	0.80	120.7	3.9
10	0.2814	0.0174	0.9036	0.0474	0.0259	0.0009	0.63	117.3	5.4
11	0.4367	0.0301	1.9547	0.1623	0.0330	0.0018	0.66	109.2	11.3
12	0.4134	0.0277	1.5193	0.0632	0.0318	0.0012	0.91	111.0	7.5
13	0.1636	0.0086	0.4884	0.0188	0.0229	0.0005	0.61	125.1	3.4
14	0.2364	0.0104	0.7566	0.0281	0.0244	0.0007	0.72	119.6	4.1
15	0.2455	0.0192	0.6450	0.0320	0.0222	0.0008	0.69	107.2	4.8
16	0.4707	0.0257	1.9566	0.0717	0.0333	0.0010	0.86	101.1	6.5
17	0.4220	0.0347	1.2847	0.0570	0.0290	0.0012	0.89	99.4	7.2
18	0.4063	0.0502	3.0899	0.2263	0.0416	0.0026	0.86	147.4	16.2
19	0.6842	0.0661	3.9290	0.1787	0.0524	0.0024	0.99	70.4	14.5
Hydrothermal monazite									
1	0.1665	0.0250	0.4325	0.0443	0.0216	0.0012	0.55	117.3	7.6
2	0.1043	0.0149	0.2680	0.0294	0.0203	0.0007	0.30	120.6	4.2
3	0.5016	0.0710	2.0192	0.2391	0.0380	0.0033	0.73	102.8	20.4
4	0.4416	0.0742	1.9995	0.2439	0.0360	0.0026	0.60	114.9	16.4
5	0.6665	0.0535	6.8691	0.4026	0.0806	0.0038	0.81	110.1	22.8
6	0.5684	0.0582	3.6402	0.3118	0.0542	0.0030	0.65	117.1	18.4
7	0.5088	0.0335	3.0583	0.1813	0.0454	0.0019	0.72	120.0	12.0
8	0.2305	0.0216	0.7186	0.0597	0.0241	0.0011	0.56	118.1	7.0
9	0.6125	0.0599	3.9060	0.2581	0.0598	0.0029	0.73	107.9	17.5
10	0.2241	0.0256	0.8614	0.1738	0.0234	0.0020	0.42	116.0	12.6
11	0.4499	0.0262	2.3441	0.1800	0.0387	0.0018	0.62	120.9	11.4
12	0.4165	0.0691	1.7802	0.4106	0.0365	0.0039	0.47	124.1	24.4
13	0.2326	0.0330	0.8270	0.1462	0.0261	0.0016	0.35	127.4	10.0
14	0.2546	0.0323	0.8865	0.1923	0.0253	0.0020	0.36	119.0	12.5
15	0.2728	0.0438	0.7743	0.0685	0.0248	0.0011	0.50	113.4	6.9
16	0.3956	0.0681	1.5283	0.1612	0.0322	0.0021	0.62	114.9	13.1
17	0.2882	0.0314	1.1070	0.1890	0.0273	0.0021	0.45	121.1	13.0
18	0.5109	0.0831	2.0165	0.2047	0.0396	0.0032	0.79	104.3	19.8
19	0.6057	0.1017	3.6096	0.3799	0.0574	0.0056	0.92	106.8	33.9

Fig. 1

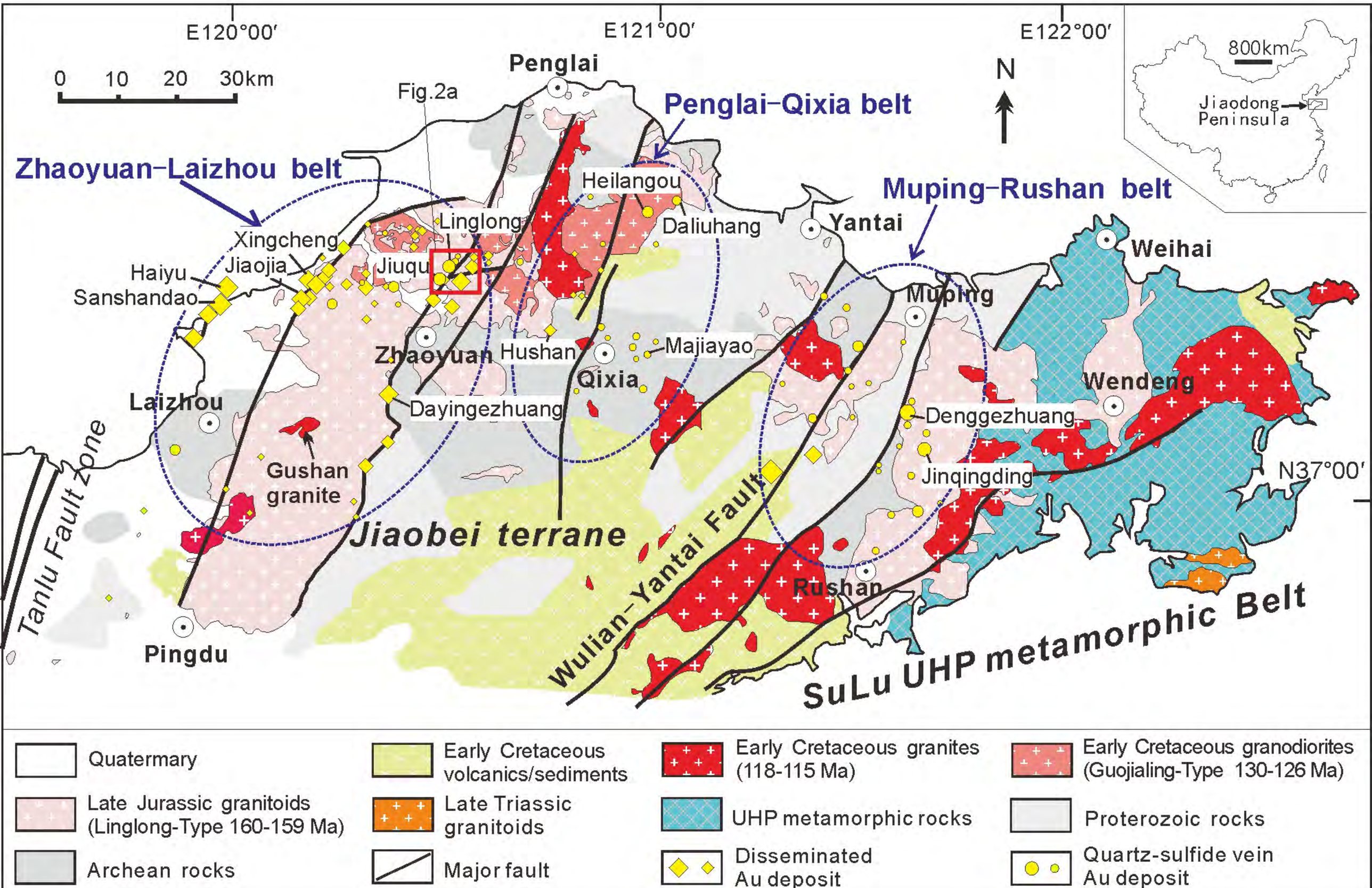
E120°00′
E121°00′
E122°00′
0 10 20 30km
N
800km
Jiaodong Peninsula
Penglai
Fig.2a
Penglai–Qixia belt
Zhaoyuan–Laizhou belt
Muping–Rushan belt
Heilangou
Linglong
Daliuhang
Yantai
Xingcheng
Jiaojia
Jiuqu
Haiyu
Sanshandao
Weihai
Muping
Zhaoyuan
Hushan
Majiayao
Qixia
Wendeng
Laizhou
Dayingezhuang
Denggezhuang
Jinqingding
N37°00′
Gushan granite
Tanlu Fault Zone
Jiaobei terrane
Wulian–Yantai Fault
Rushan
Pingdu
SuLu UHP metamorphic Belt
Quatermary
Early Cretaceous volcanics/sediments
Early Cretaceous granites (118-115 Ma)
Early Cretaceous granodiorites (Guojialing-Type 130-126 Ma)
Late Jurassic granitoids (Linglong-Type 160-159 Ma)
Late Triassic granitoids
UHP metamorphic rocks
Proterozoic rocks
Archean rocks
Major fault
Disseminated Au deposit
Quartz-sulfide vein Au deposit

Fig. 2

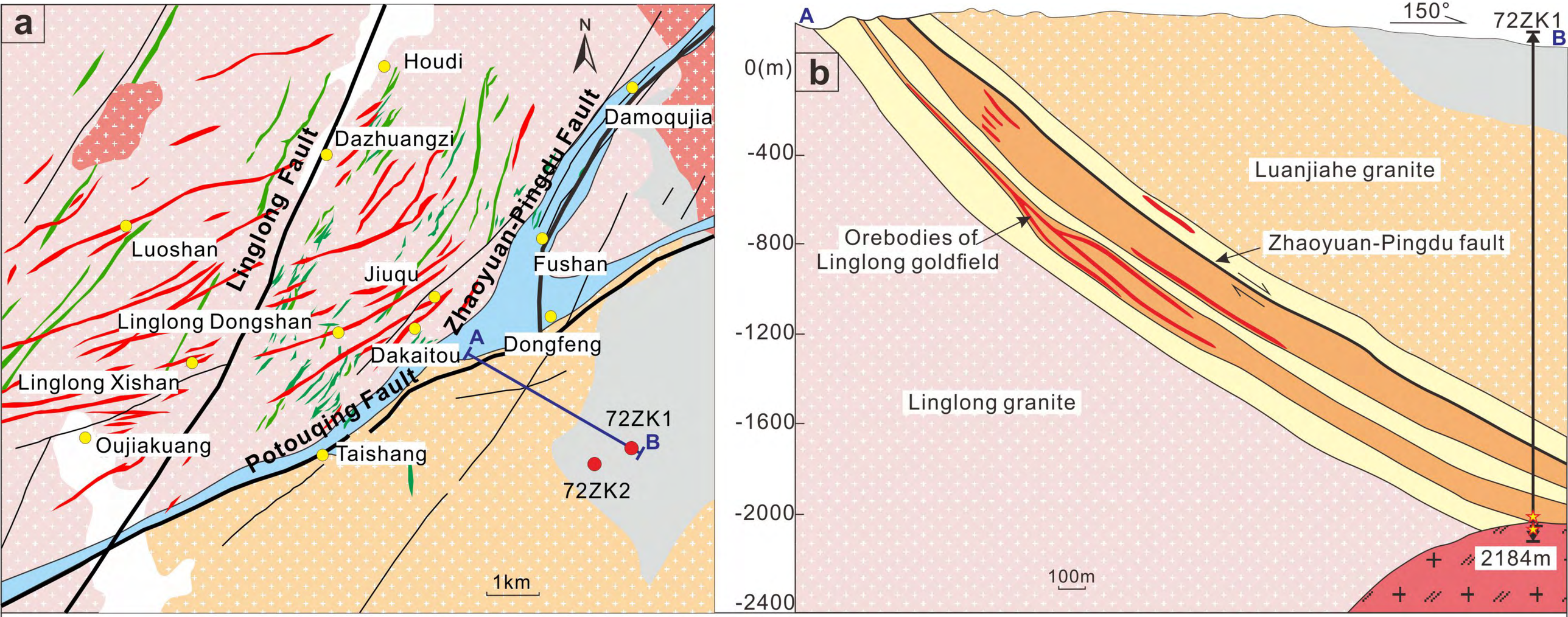
a
N
Houdi
Damoqujia
Dazhuangzi
Linglong Fault
Zhaoyuan-Pingdu Fault
Luoshan
Fushan
Jiuqu
Linglong Dongshan
Dakaitou
A
Dongfeng
Linglong Xishan
72ZK1
B
Oujiakuang
Potouqing Fault
Taishang
72ZK2
1km
b
A
150°
72ZK1
B
0(m)
-400
-800
-1200
-1600
-2000
-2400
Luanjiahe granite
Orebodies of
Linglong goldfield
Zhaoyuan-Pingdu fault
Linglong granite
2184m
100m
Quaternary
Biotite monzonite
Early Cretaceous
Guojialing granodiorite
Late Jurassic
Linglong granite
Late Jurassic
Luanjiahe granite
Jiaodong group
Sample
K-feldspar
alteration
Sericitization
Dike
Fault
Orebody
Cataclastic zone
Gold deposit
Drilling hole

Fig. 3

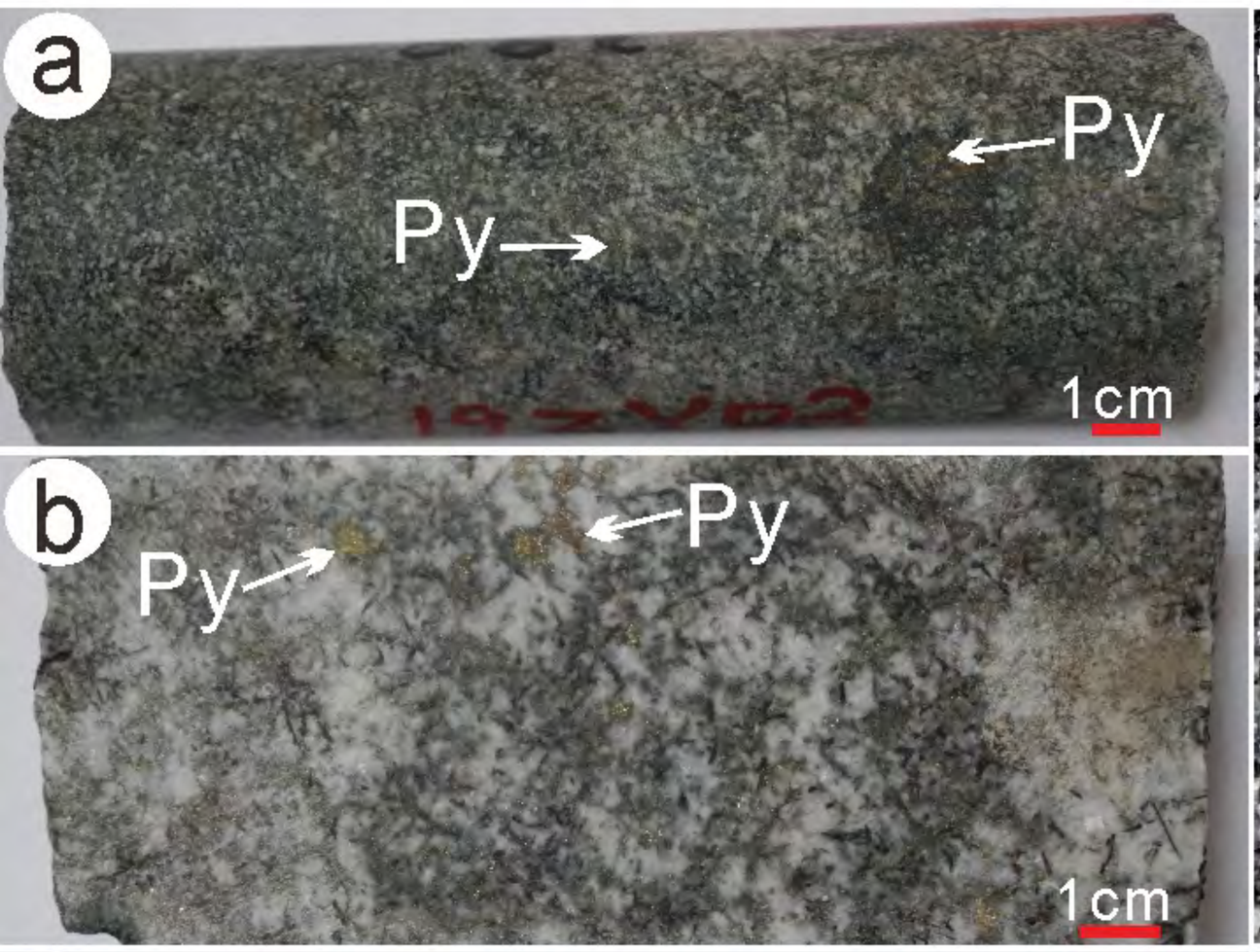
a
Py
Py
1cm

b
Py
Py
1cm

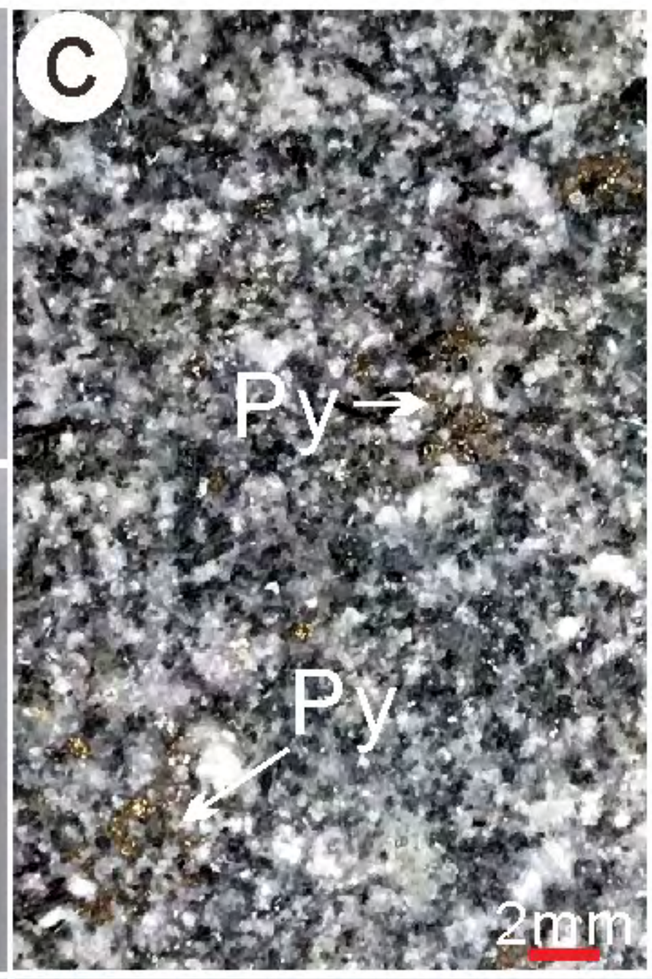
c
Py
Py
2mm

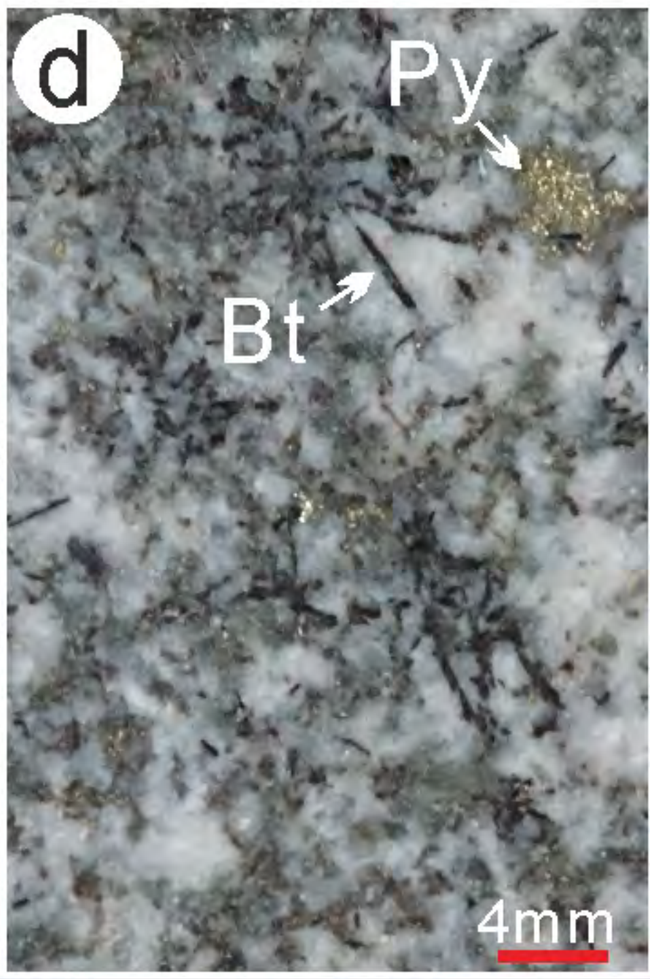
d
Py
Bt
4mm

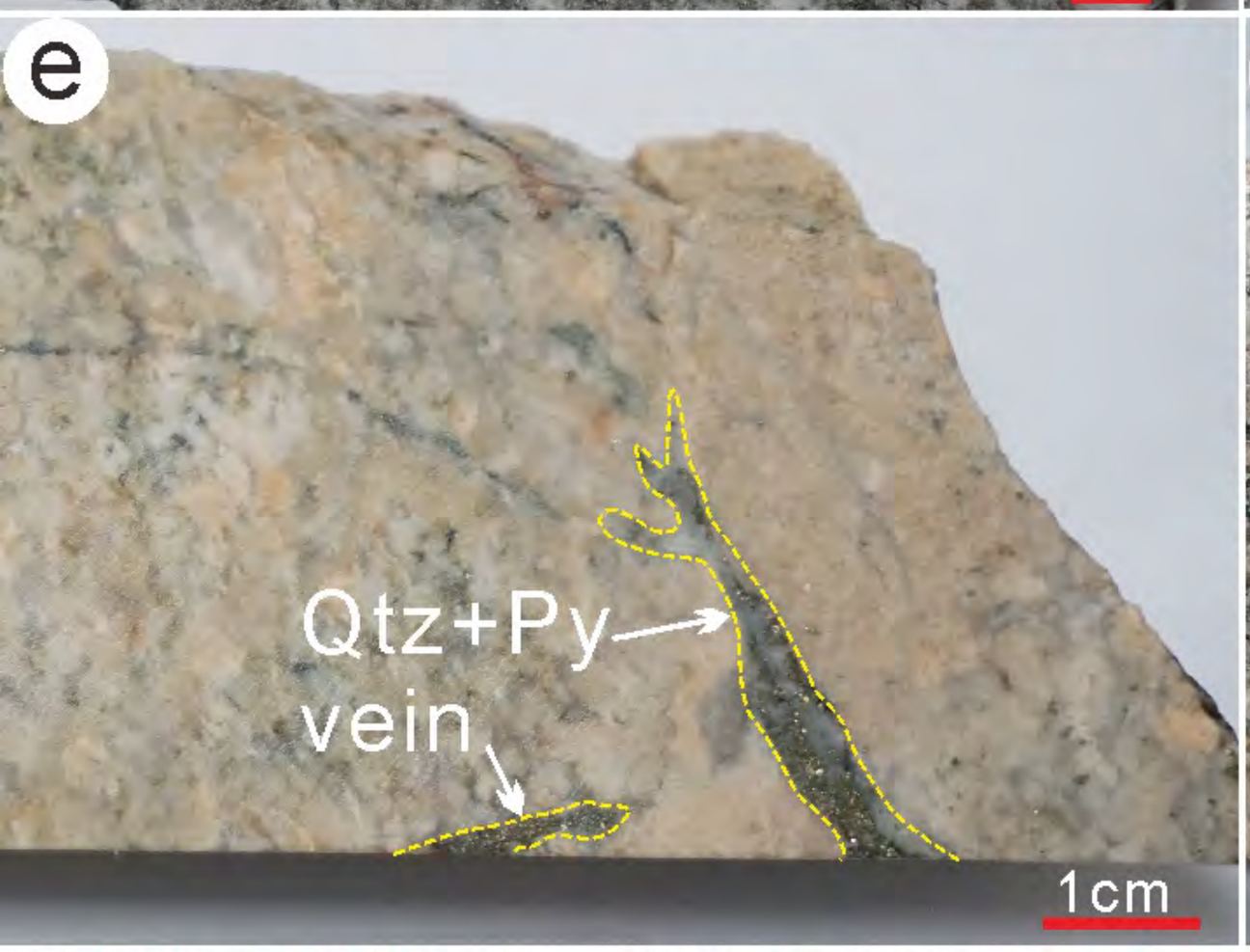
e
Qtz+Py
vein
1cm

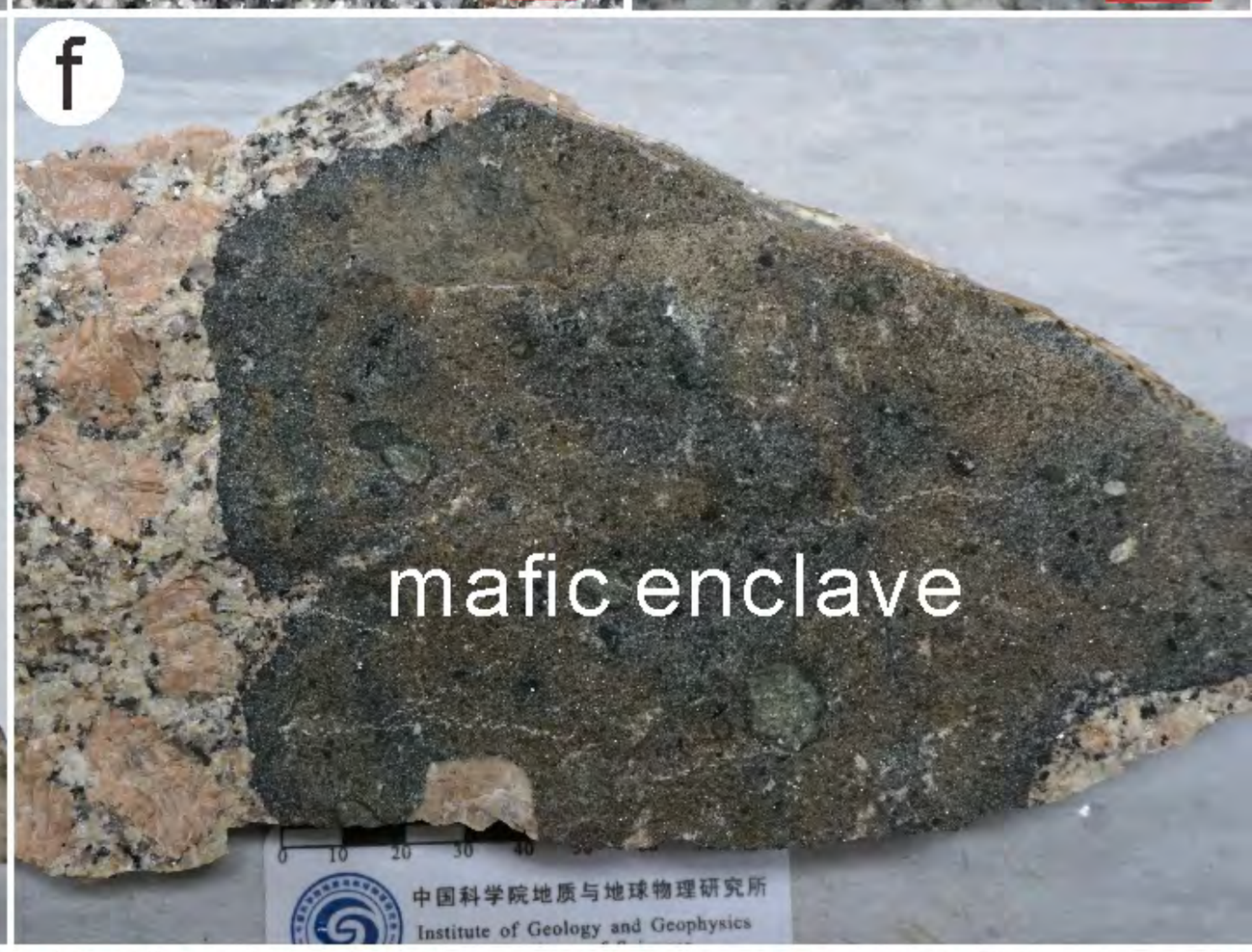
f
mafic enclave
中国科学院地质与地球物理研究所
Institute of Geology and Geophysics

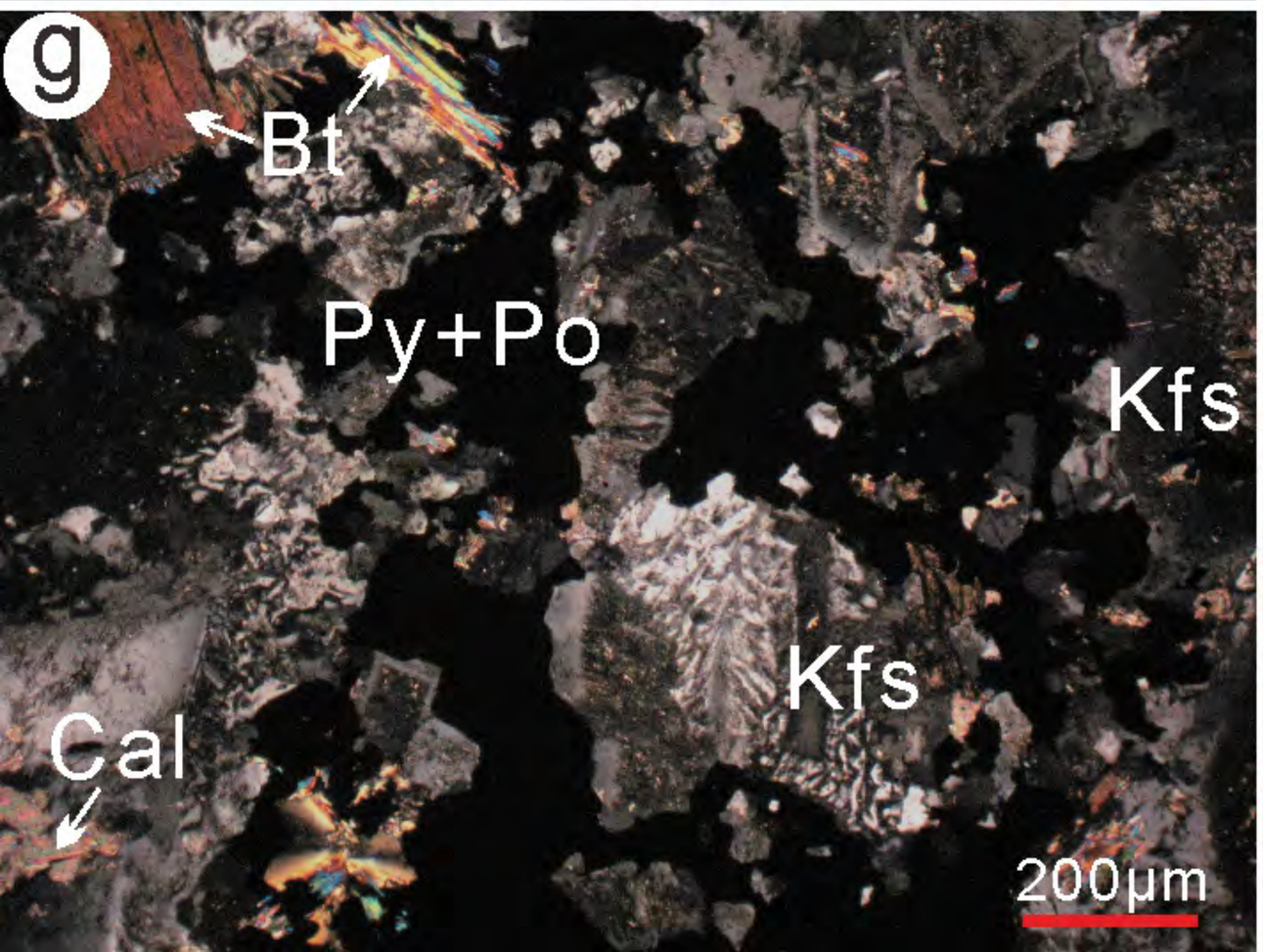
g
Bt
Py+Po
Kfs
Kfs
Cal
200μm

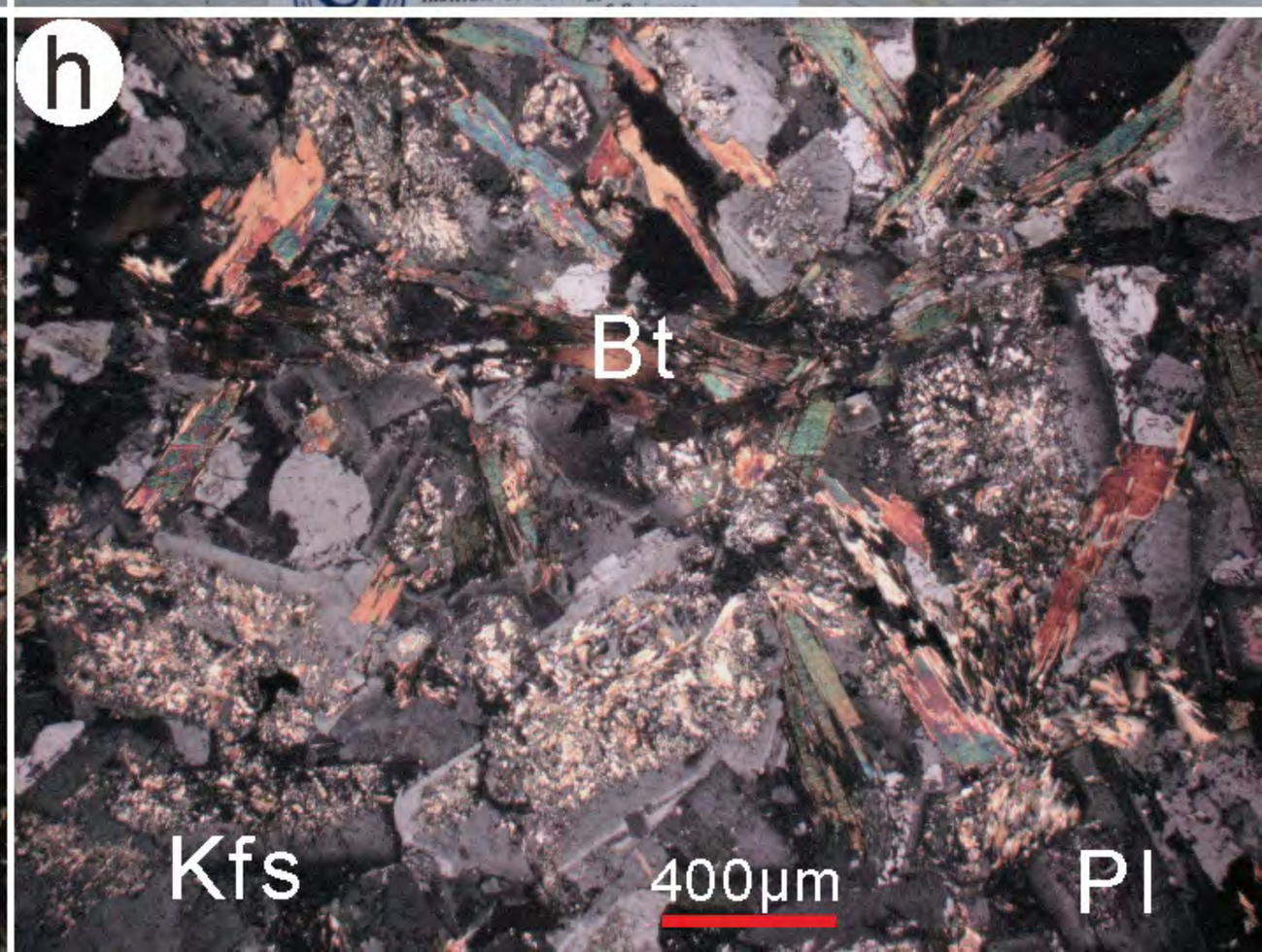
h
Bt
Kfs
400μm
Pl

Fig. 4

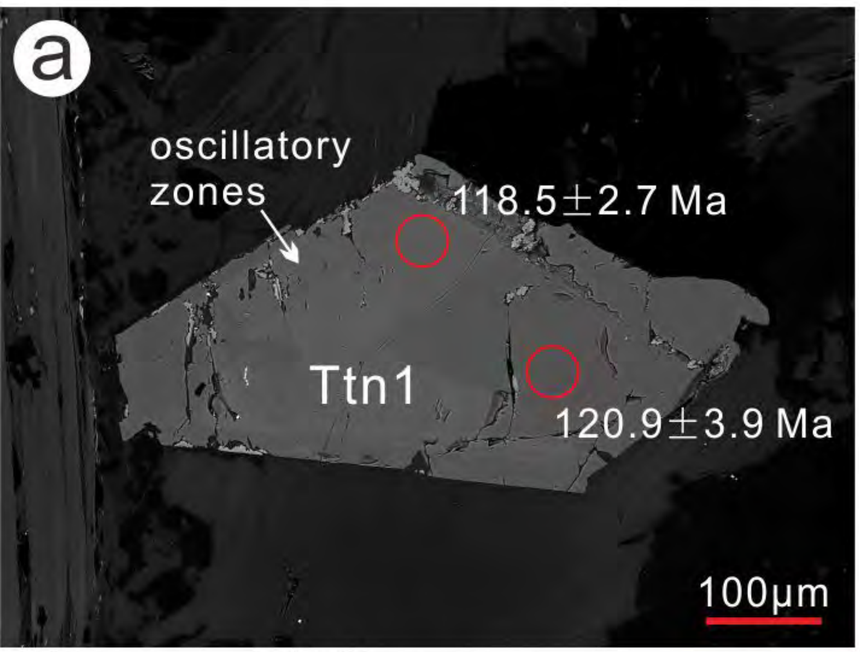
a
oscillatory
zones
118.5±2.7 Ma
Ttn1
120.9±3.9 Ma
100μm

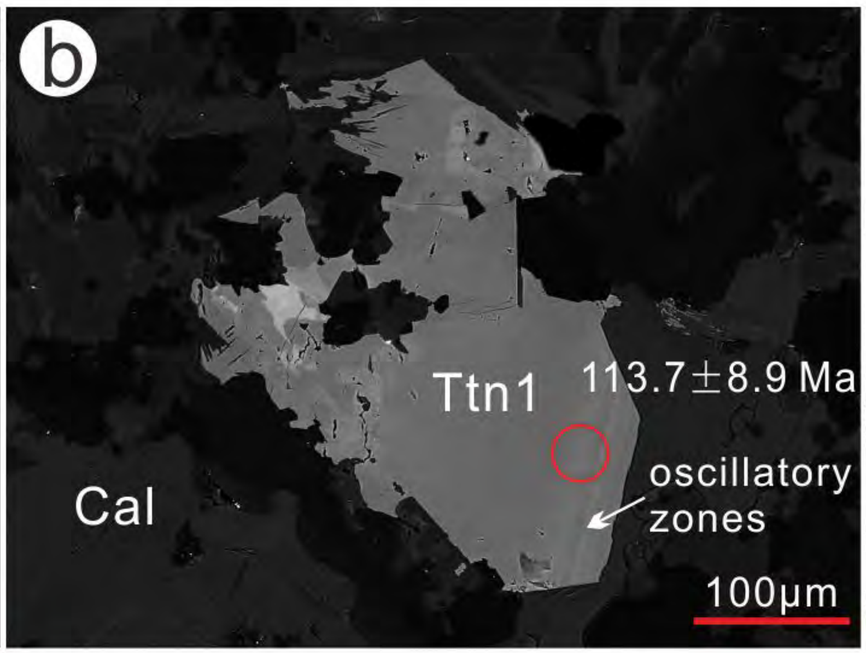
b
Ttn1
113.7±8.9 Ma
Cal
oscillatory
zones
100μm

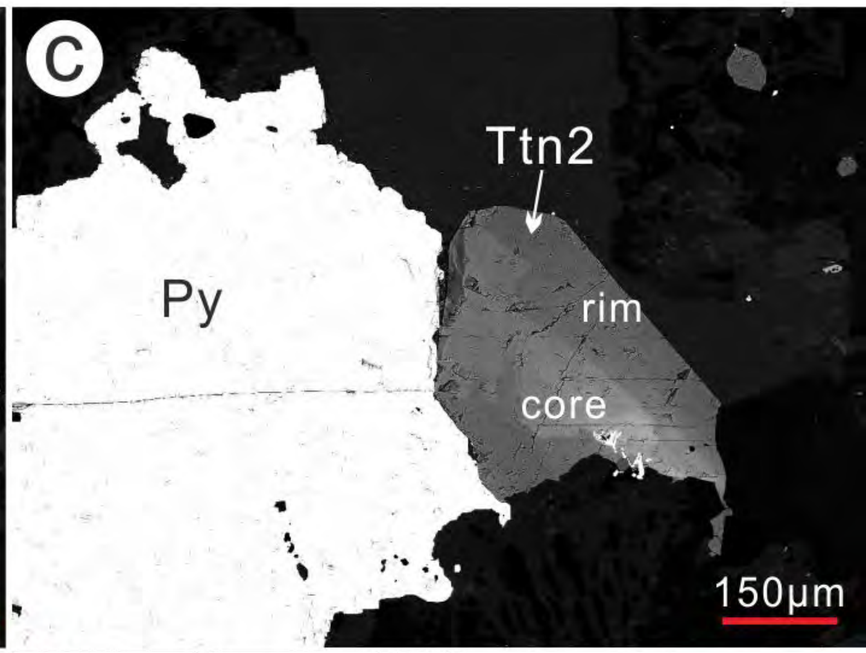
c
Ttn2
Py
rim
core
150μm

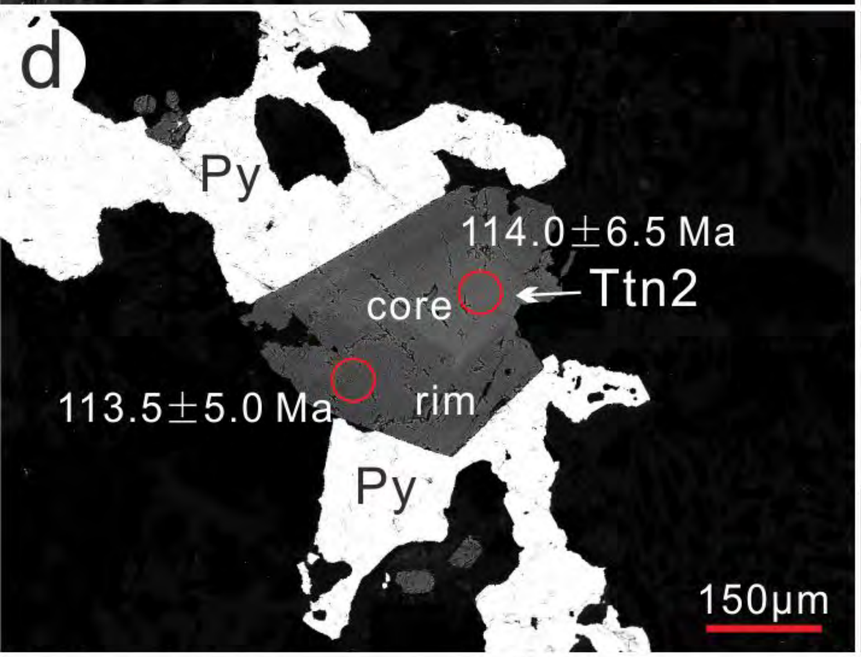
d
Py
114.0±6.5 Ma
core
Ttn2
113.5±5.0 Ma
rim
Py
150μm

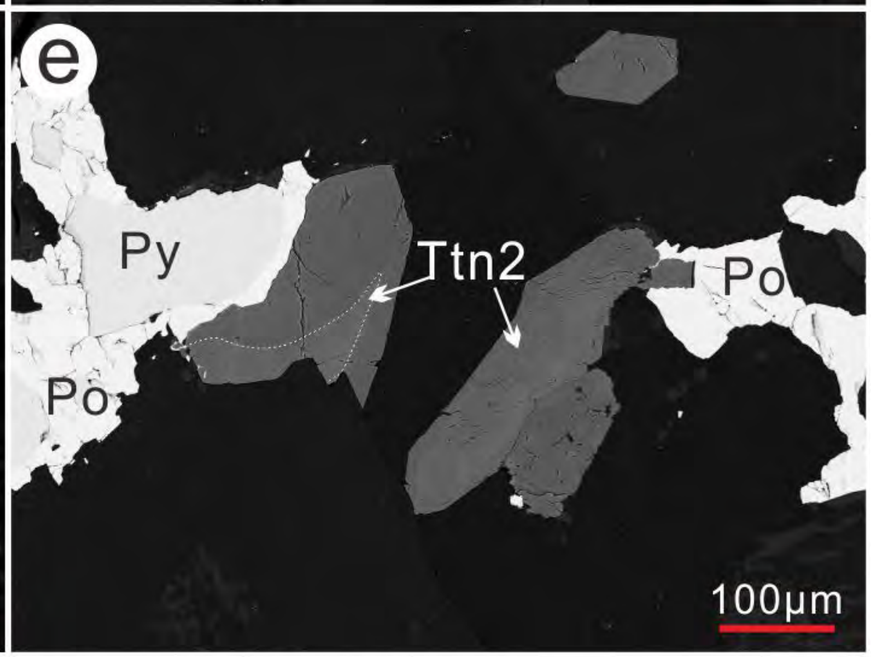
e
Py
Ttn2
Po
Po
100μm

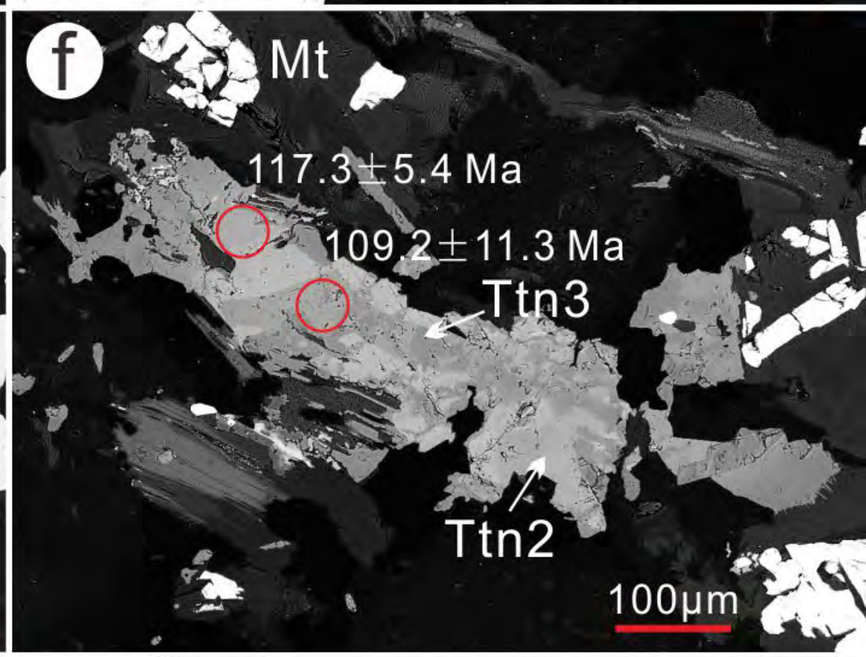
f
Mt
117.3±5.4 Ma
109.2±11.3 Ma
Ttn3
Ttn2
100μm

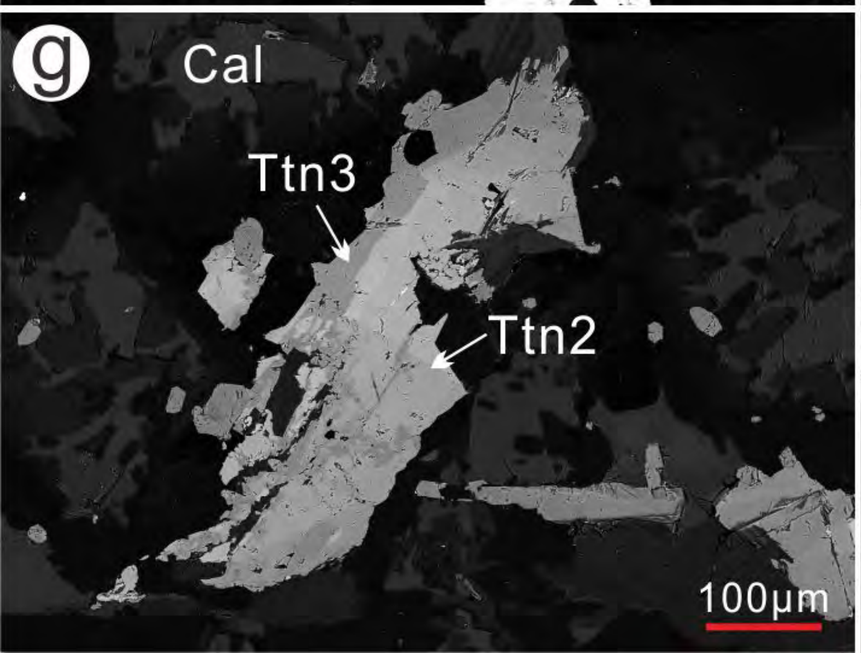
g
Cal
Ttn3
Ttn2
100μm

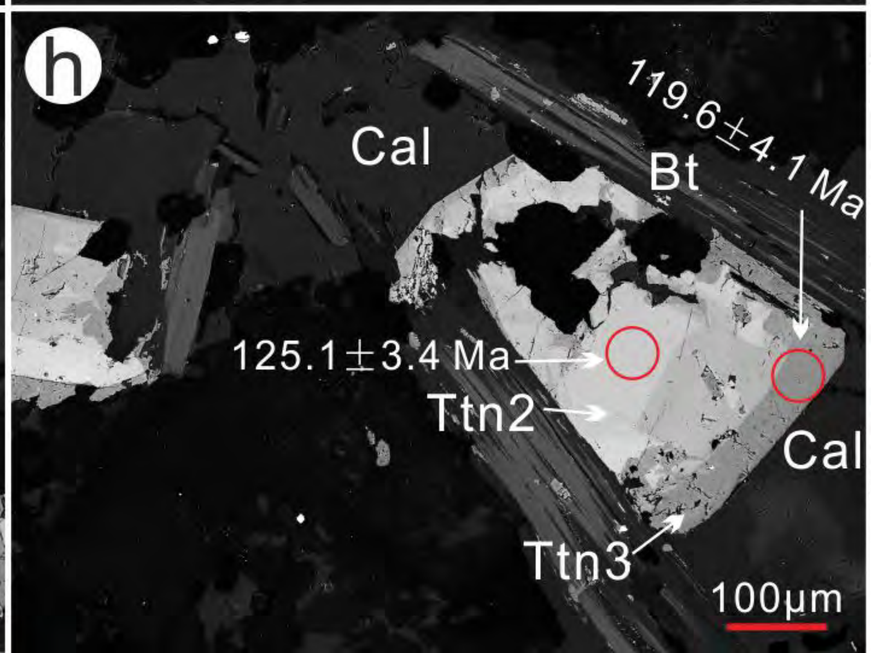
h
Cal
Bt
119.6±4.1 Ma
125.1±3.4 Ma
Ttn2
Cal
Ttn3
100μm

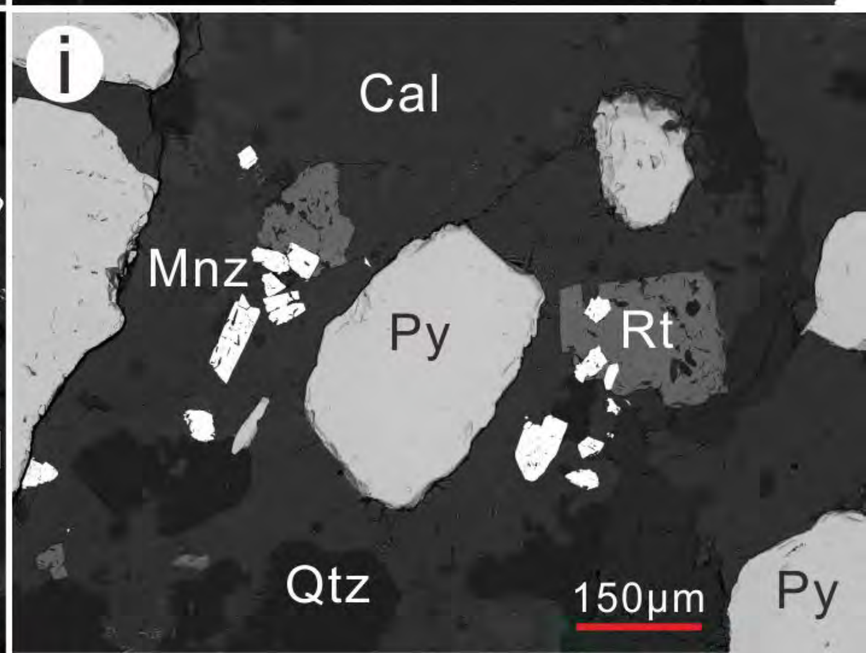
i
Cal
Mnz
Py
Rt
Qtz
150μm
Py

Fig. 5

a
Ttn1
Ttn2
Ttn3
TiO2 (wt.%)
FeO (wt.%)
b
MnO (wt.%)
c
CaO (wt.%)
REE (ppm)
d
LREE/HREE
e
Eu_N/Eu_N*
Lu/Hf
f
Th (ppm)
Pb (ppm)

Fig. 6

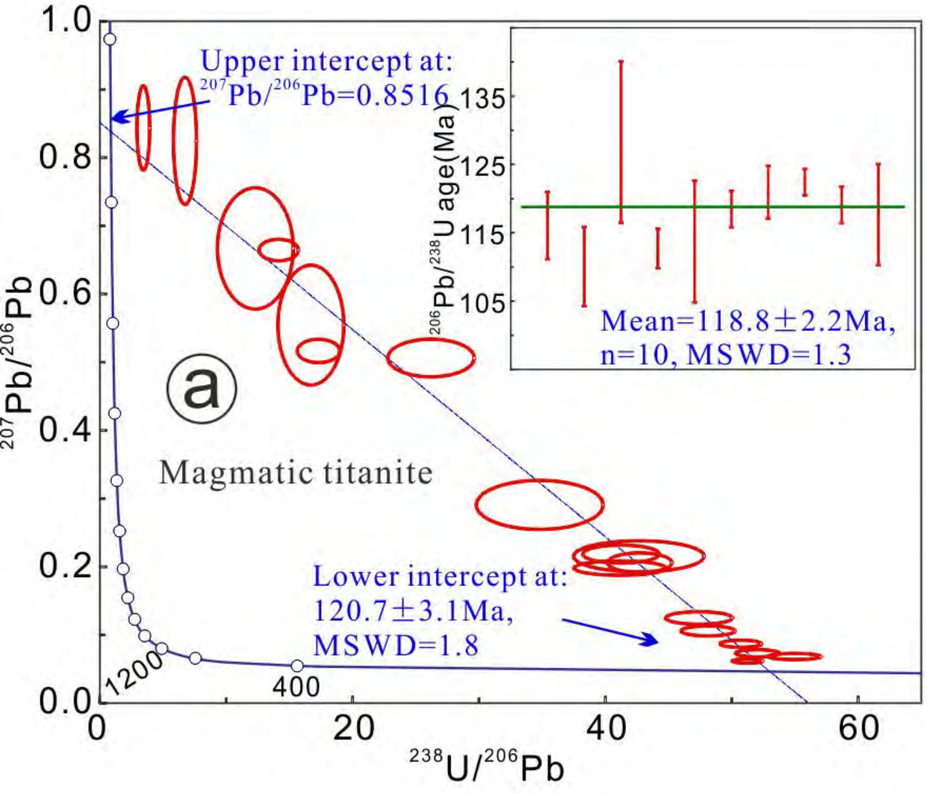
Upper intercept at:
$^{207}Pb/^{206}Pb$=0.8516
$^{206}Pb/^{238}U$ age(Ma)
Mean=118.8±2.2Ma,
n=10, MSWD=1.3
a
Magmatic titanite
Lower intercept at:
120.7±3.1Ma,
MSWD=1.8
1200
400
$^{207}Pb/^{206}Pb$
$^{238}U/^{206}Pb$

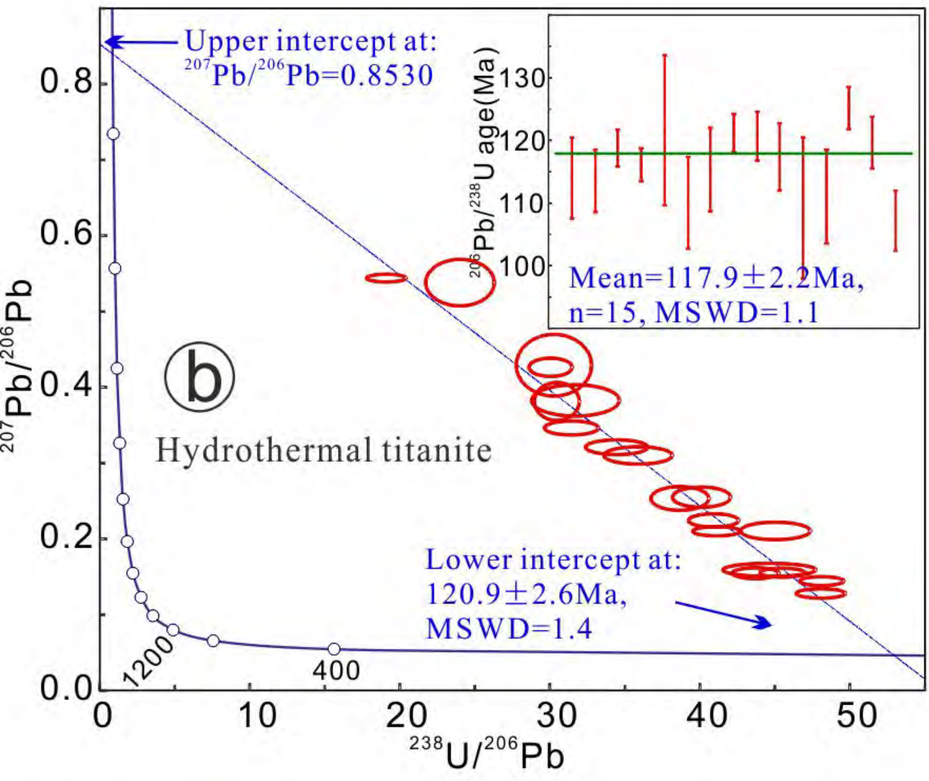
Upper intercept at:
$^{207}Pb/^{206}Pb$=0.8530
$^{206}Pb/^{238}U$ age(Ma)
Mean=117.9±2.2Ma,
n=15, MSWD=1.1
b
Hydrothermal titanite
Lower intercept at:
120.9±2.6Ma,
MSWD=1.4
1200
400
$^{207}Pb/^{206}Pb$
$^{238}U/^{206}Pb$

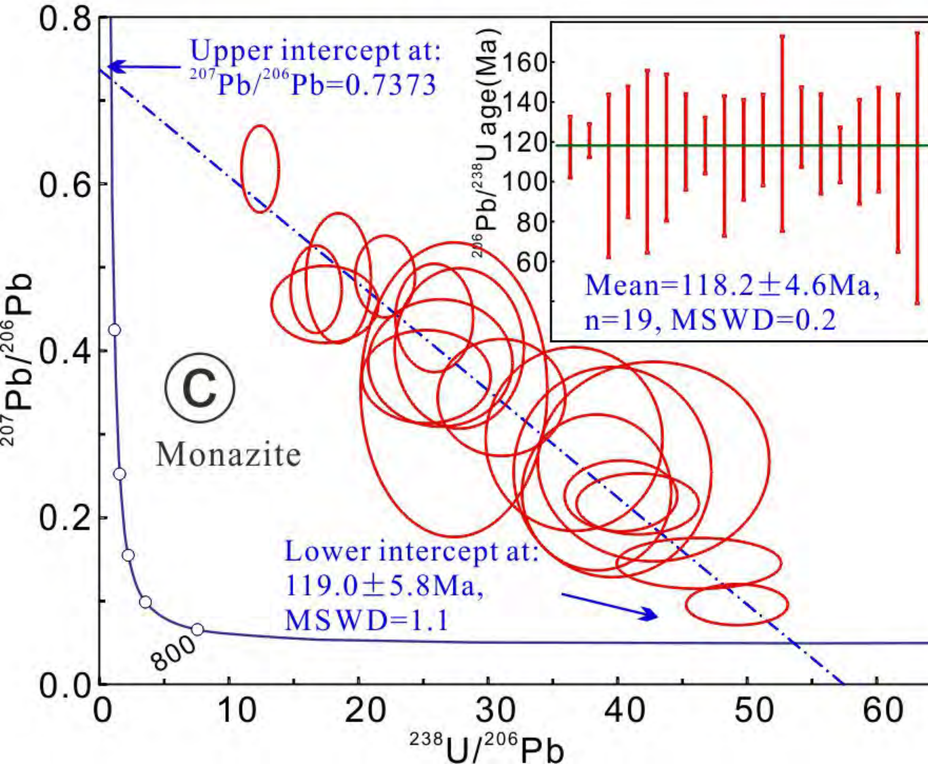
Upper intercept at:
$^{207}Pb/^{206}Pb$=0.7373
$^{206}Pb/^{238}U$ age(Ma)
Mean=118.2±4.6Ma,
n=19, MSWD=0.2
c
Monazite
Lower intercept at:
119.0±5.8Ma,
MSWD=1.1
800
$^{207}Pb/^{206}Pb$
$^{238}U/^{206}Pb$

Fig. 7

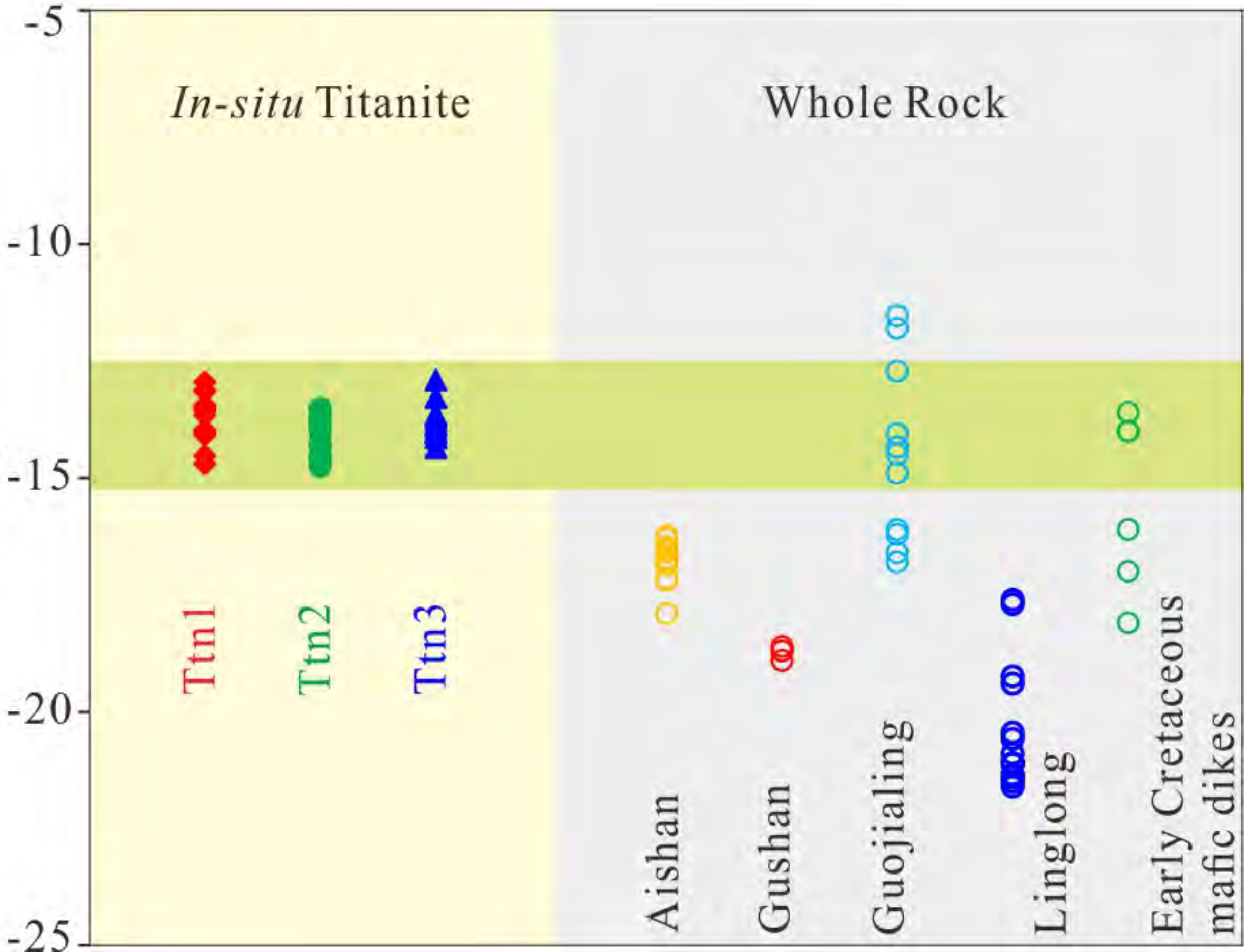
-5
-10
-15
-20
-25
εNd(t)
In-situ Titanite
Whole Rock
Ttn1
Ttn2
Ttn3
Aishan
Gushan
Guojialing
Linglong
Early Cretaceous mafic dikes

Fig. 8

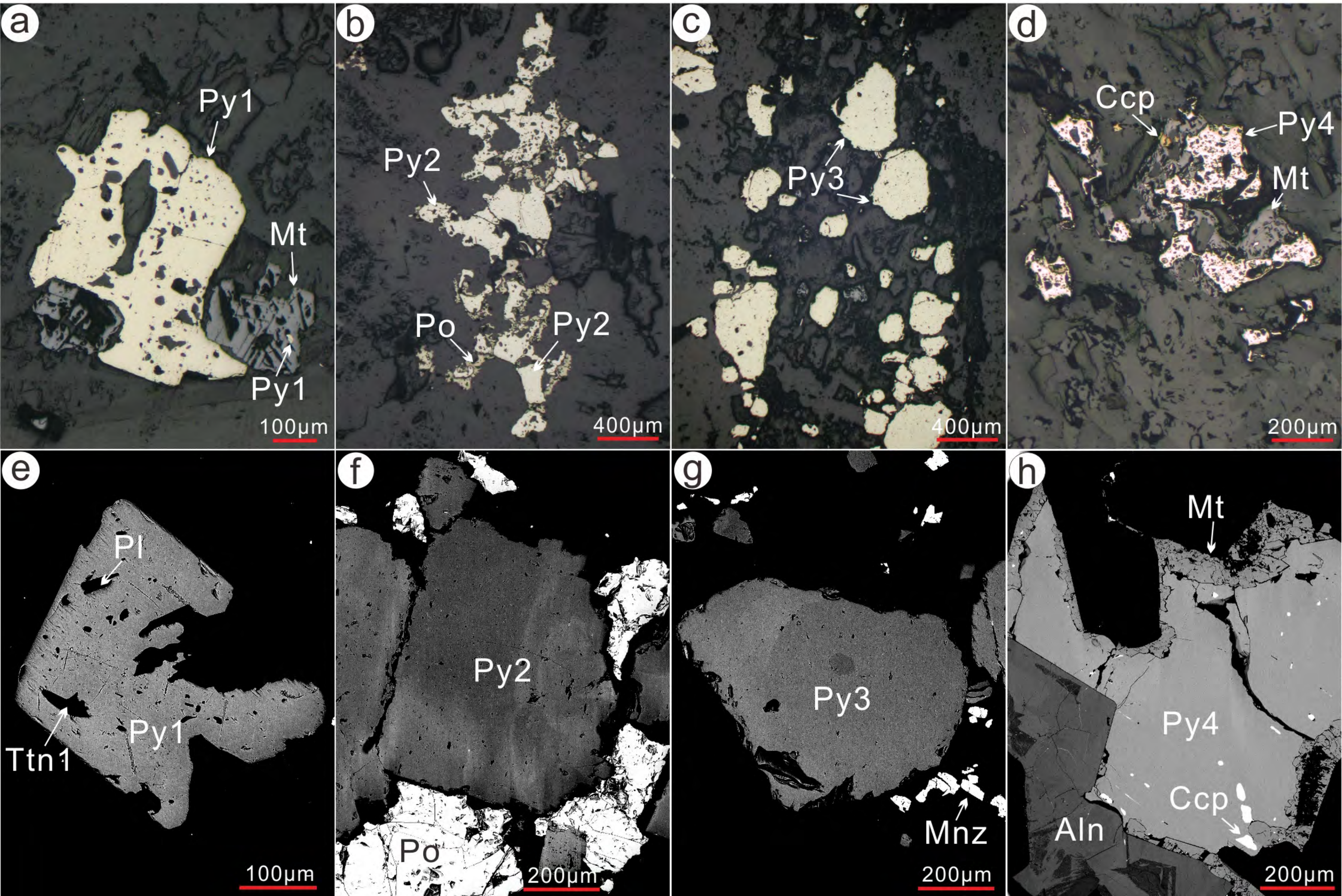
a
Py1
Mt
Py1
100μm
b
Py2
Po
Py2
400μm
c
Py3
400μm
d
Ccp
Py4
Mt
200μm
e
Pl
Py1
Ttn1
100μm
f
Py2
Po
200μm
g
Py3
Mnz
200μm
h
Mt
Py4
Ccp
Aln
200μm

Fig. 9

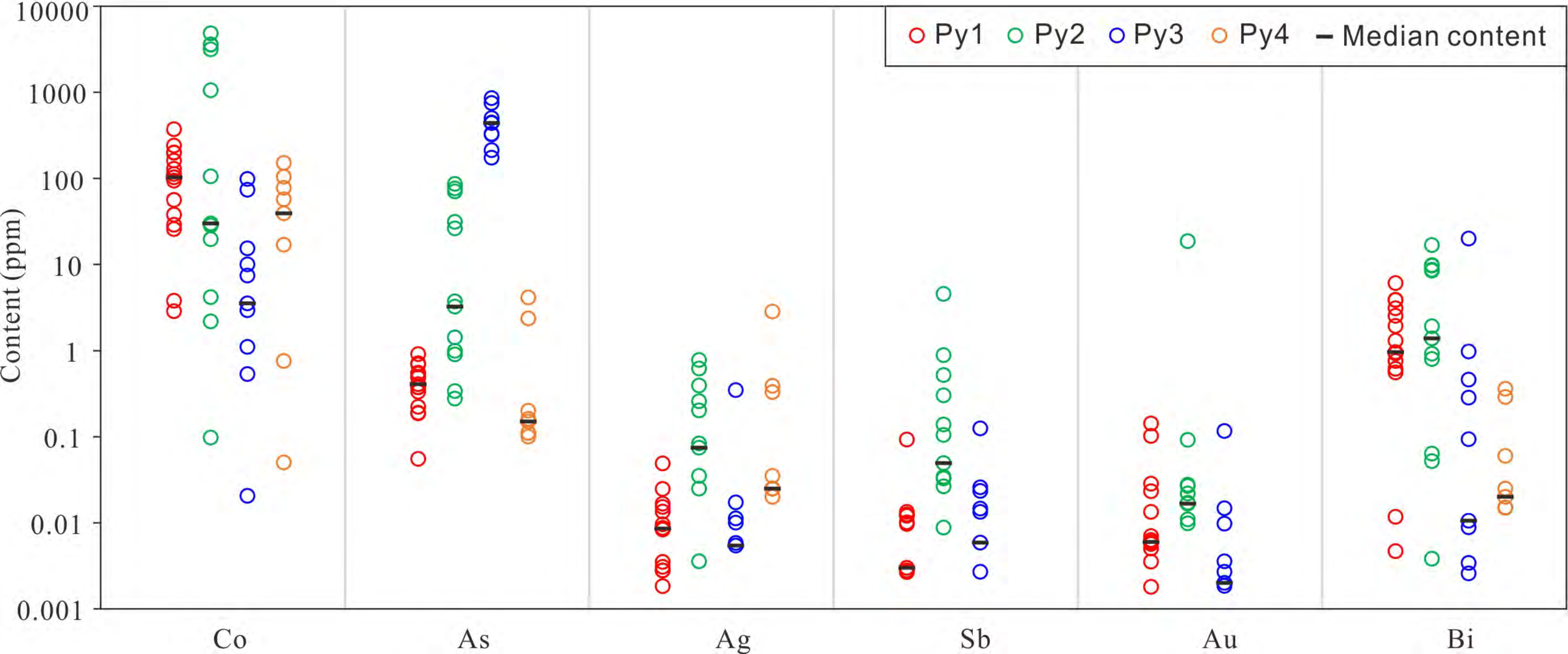
Py1
Py2
Py3
Py4
Median content
Content (ppm)
10000
1000
100
10
1
0.1
0.01
0.001
Co
As
Ag
Sb
Au
Bi

Fig. 10

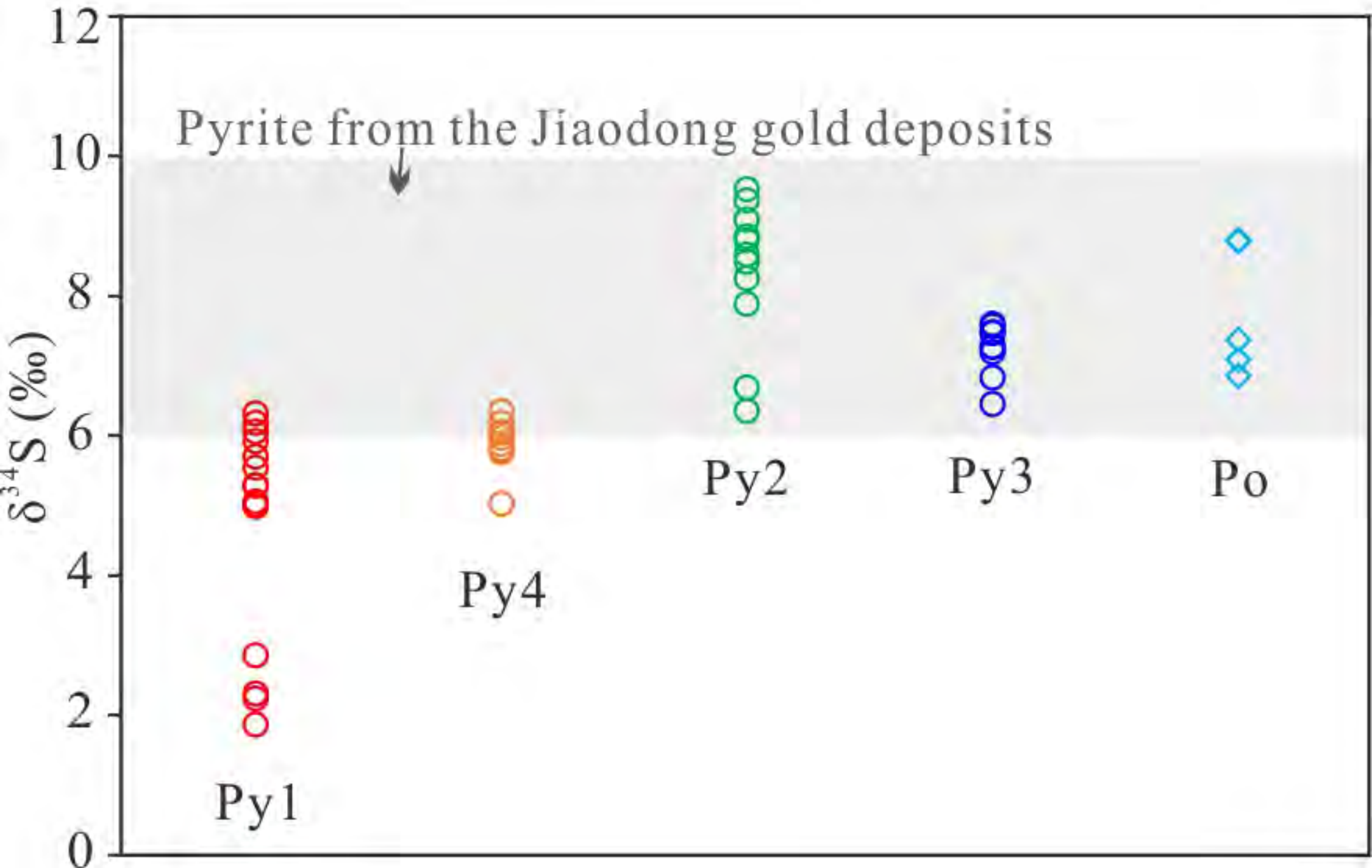
Pyrite from the Jiaodong gold deposits
$\delta^{34}S$ (‰)
12
10
8
6
4
2
0
Py1
Py4
Py2
Py3
Po

Fig. 11

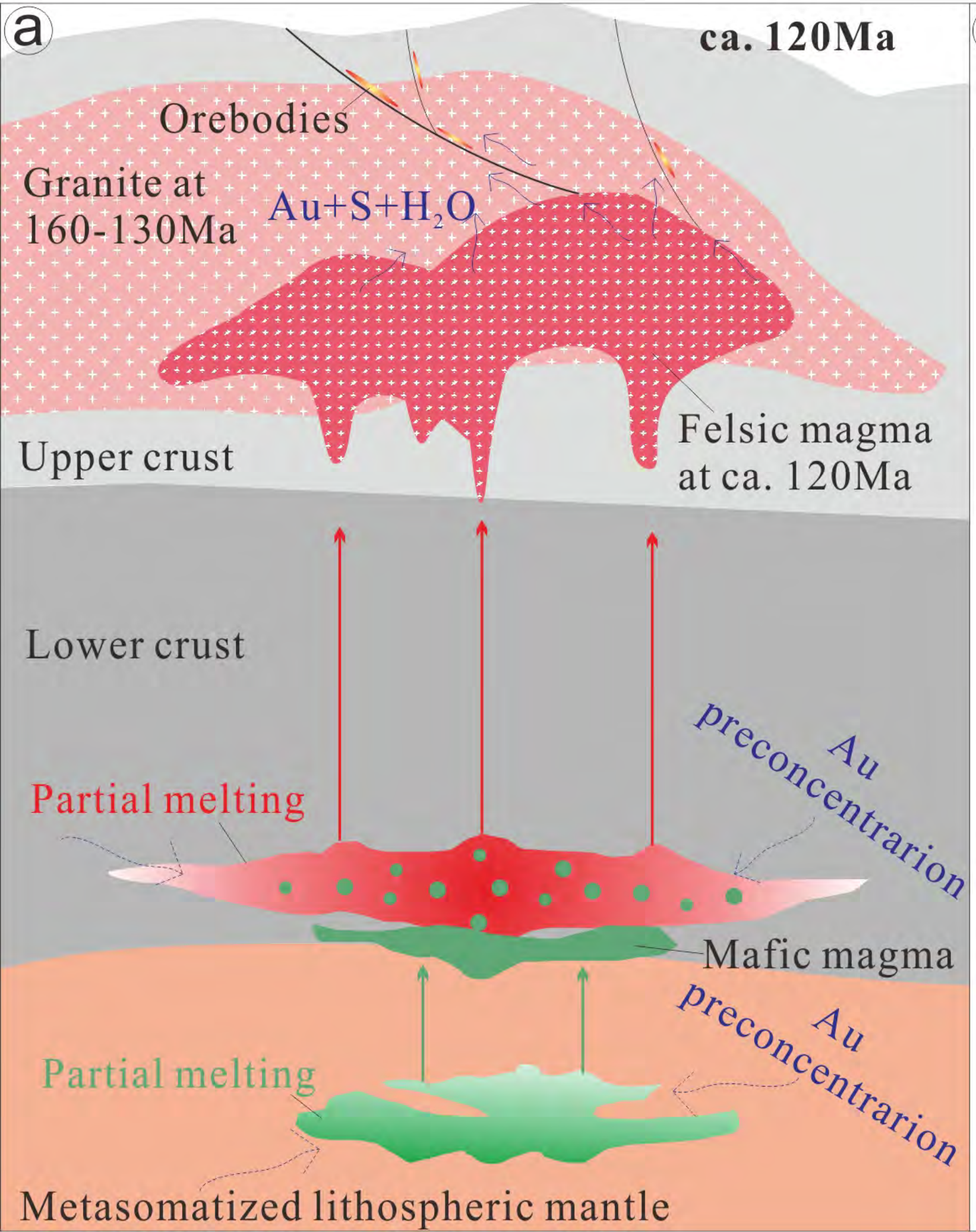
a
ca. 120Ma
Orebodies
Granite at
160-130Ma
Au+S+H2O
Upper crust
Felsic magma
at ca. 120Ma
Lower crust
Au
preconcentrarion
Partial melting
Mafic magma
Au
preconcentrarion
Partial melting
Metasomatized lithospheric mantle

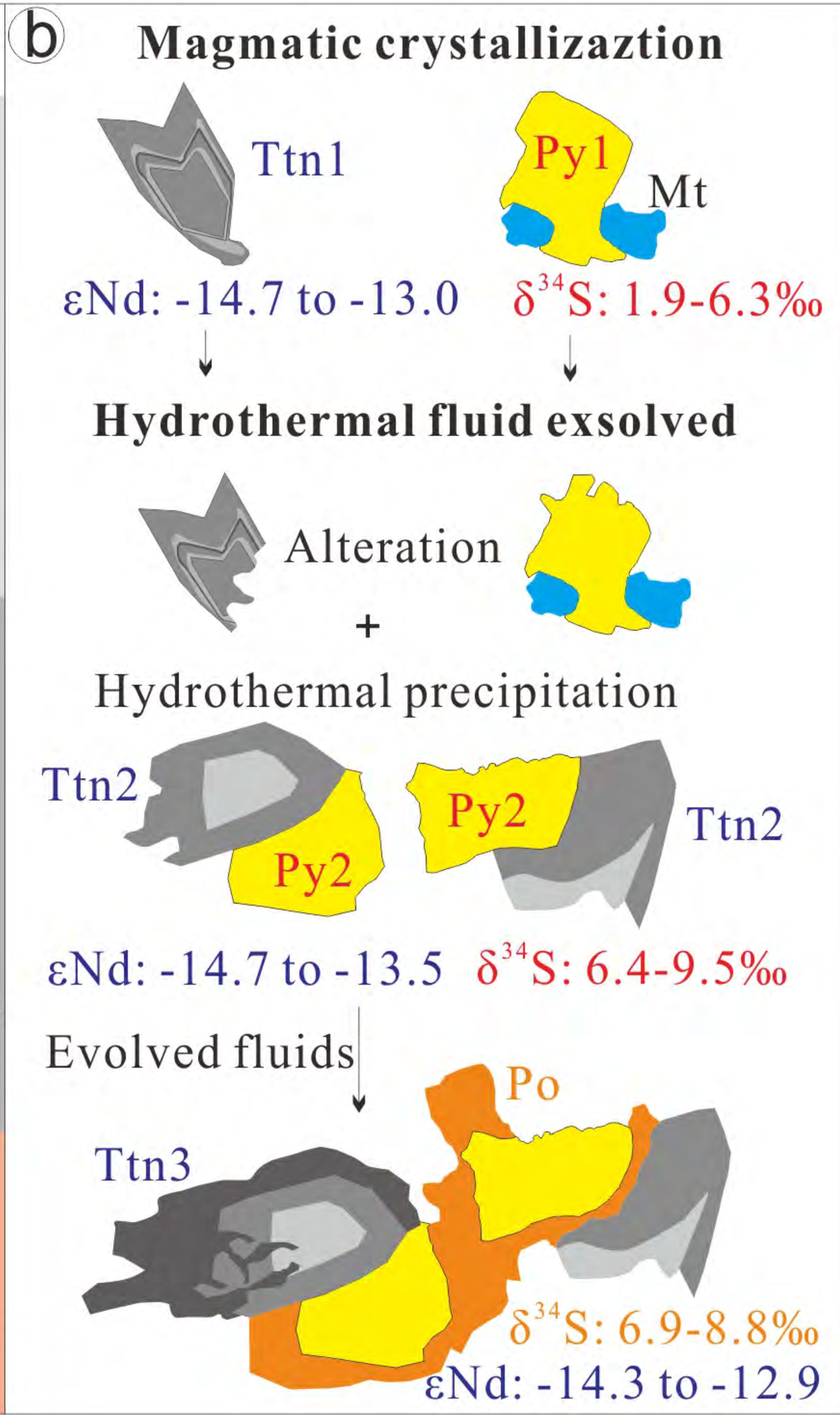
b
Magmatic crystallizaztion
Ttn1
Py1
Mt
εNd: -14.7 to -13.0
δ34S: 1.9-6.3‰
Hydrothermal fluid exsolved
Alteration
+
Hydrothermal precipitation
Ttn2
Py2
Py2
Ttn2
εNd: -14.7 to -13.5
δ34S: 6.4-9.5‰
Evolved fluids
Po
Ttn3
δ34S: 6.9-8.8‰
εNd: -14.3 to -12.9